Revision 1, manuscript #5530

Exploring the potential of Raman spectroscopy for crystallochemical analyses of complex hydrous silicates: II. Tourmalines

Anke Watenphul[1*], Martina Burgdorf[1], Jochen Schlüter[2], Ingo Horn[3], Thomas Malcherek[1], and Boriana Mihailova[1]

[1]Fachbereich Geowissenschaften, Universität Hamburg, Grindelallee 48, D-20146 Hamburg, Germany

[2]Centrum für Naturkunde, Mineralogisches Museum, Universität Hamburg, Grindelallee 48, D-20146 Hamburg

[3]Institut für Mineralogie, Leibniz Universität Hannover, Callinstr. 3, D-30167 Hannover 30167, Germany

[*]corresponding author: anke.watenphul@uni-hamburg.de

ABSTRACT

A detailed Raman spectroscopic, electron microprobe, and laser ablation induced-coupled plasma mass spectrometric study of forty-six natural tourmalines ($XY_3Z_6(T_6O_{18})(BO_3)_3V_3W$) from ten subgroups was performed to evaluate the potential of the Raman scattering, in particular of the OH bond stretching vibrations, for the identification of tourmaline species and site-occupancy analysis. The widespread chemical variety of the studied samples is reflected in the different spectral shapes. The positions and intensities of the observed vibrational modes can be used for tourmaline species identification. Taking into account the charge of the Y and Z-site cations as well as the X-site occupancy, the Raman peaks generated by the bond stretching mode of the ^{V}OH groups were attributed to different YZZ-YZZ-YZZ cationic configurations, while the peaks originating from ^{W}OH stretching to chemically different YYY triplets next to an X-site vacancy, ^{X}Na, or ^{X}Ca. It is shown that the integrated intensities of the ^{V}OH-stretching peaks can be used to calculate the contents of the major Y-site elements Mg, (Fe^{2+}+Mn^{2+}), Li, and Al. The

analysis of the ^{V}OH-peak positions yields information on the X-site occupancy. The fitted linear equations can be used to determine the content of ^{X}(Na+Ca) and X-site vacancy per formula unit. Guidelines how to gain crystallochemical information from the Raman spectra of tourmaline, are suggested. This study, along with Part 1 dedicated to amphiboles (Leißner et al. 2015), reveals that Raman spectroscopy is well suited as a non-destructive, preparation-free, and easy-to-handle method for species identification and site-occupancy analysis in complex hydrous silicate. Our results demonstrate that the chemistry on the non-tetrahedral positions substantially influences the Raman-active H-O bond stretching phonon modes, which allows for quantitative compositional analysis, including the content of lithium.

Keywords: tourmaline, Raman spectroscopy, electron microprobe analysis, LA-ICP-MS

INTRODUCTION

Tourmalines are hydrous borosilicates with complex chemical composition, which form a mineral supergroup. The majority of tourmalines exhibit rhombohedral symmetry with space group $R3m$. The general formula is $XY_3Z_6(T_6O_{18})(BO_3)_3V_3W$ with the common cations and anions at each site in order of their relative abundance (Henry et al. 2011):

$X = Na^{+}, Ca^{2+}, \square, K^{+}$ (with $\square$ as symbol for a vacant site);

$Y = Fe^{2+}, Mg^{2+}, Mn^{2+}, Al^{3+}, Li^{+}, Fe^{3+}, Cr^{3+}, Ti^{4+}, Zn^{2+}, Cu^{2+}, V^{3+}$;

$Z = Al^{3+}, Fe^{3+}, Mg^{2+}, Fe^{2+}, Cr^{3+}, V^{3+}$;

$T = Si^{4+}, Al^{3+}, B^{3+}$;

$B = B^{3+}$;

$V = (OH)^{-}, O^{2-}$; and

$W = F^{-}, (OH)^{-}, O^{2-}$.

The crystal structure of tourmaline is composed of 6-membered rings of TO_4 tetrahedra, whose apical oxygen atoms point towards the (-) *c*-pole, causing the acentric nature of the structure (Fig. 1). Triangular BO_3 groups are sub-parallel to the (001) plane and they are placed above and below the tetrahedral rings. The nine-coordinated X site is located on the three-fold axis of symmetry, out of plane of the tetrahedral rings. The two octahedrally coordinated sites Y and Z are just inside and outside with respect to the ring contour. The V site, labeled as O(3) in crystallographic data, is shared by one YO_6 and two ZO_6 octahedra. The W site, labeled as O(1) in crystallographic data, is located on the 3-fold axis central to the tetrahedral rings and linked to 3 YO_6 octahedra.

The tourmaline supergroup currently consists of thirty-two species approved by the International Mineralogical Association's Commission on New Minerals, Nomenclature and Classification. The classification is related to the dominant compositional variability that occurs at the X, Y, Z, and W site and, to lesser extent, also at the V site. The primary division is made according to the dominant X-site occupancy resulting in the three groups alkali, calcic, and X-vacant tourmaline. Secondary divisions distinguish between the dominant occupancies of the Y site considering also major variations in the Z- and T-site occupancy. Further divisions are made according to the dominant W-site occupancy resulting in

hydroxy-, fluor-, and oxy-species. Details of the most recent tourmaline classification and nomenclature are given by Henry et al. (2011).

Tourmalines crystallize in a wide range of geological settings, including hydrothermal, metamorphic, metasomatic, magmatic and as detrital grains in clastic sediments (e.g., Henry and Dutrow 1996; Slack 1996; Henry et al. 1999; Marschall et al. 2009). Within these settings, there is a large variety of host rock compositions, in which tourmalines can occur from silica-rich intrusive bodies and sediments, to silica-poor mafic rocks, pelites, impure limestones and evaporates, and their metamorphic equivalents. This widespread occurrence is enabled by the extensive pressure and temperature stability range of tourmaline (van Hinsberg et al. 2011 and references therein), which covers most of the conditions in the Earth's crust down to the upper mantle. The tourmaline stability can be partially attributed to the flexibility in its crystal structure that can adopt various compositions as a response to alternating chemical environments and pressure-temperature conditions (Dutrow and Henry 2011). The compositional changes within the same tourmaline specimen are often rather abrupt and occur within a few micrometers due to negligible diffusion rates of major and trace elements. Thus, tourmalines can be regarded as almost ideal petrogenetic indicators to their host environment as they can capture the signature of the host rock bulk composition (Henry and Dutrow 1996; Keller et al. 1999; Selway et al. 1999, 2000; Williamson et al. 2000; Henry and Dutrow 2001; London 2011; Trumbull et al. 2011; van Hinsberg et al. 2011). In addition, the systematic variations in tourmaline chemistry with the pressure and temperature of the host environment (Henry and Dutrow 1996; Ertl et al. 2008, 2010) have been used to calibrate tourmalines for geothermometry (Colopietro and Friberg 1987; Henry and Dutrow 1996; Kawakami and Ikeda 2003; van Hinsberg and Schumacher 2007).

Hence, the identification of different tourmaline species and their crystal chemistry is of great importance to access all that information. As zonation in tourmalines often occurs on a fine length scale (Hawthorne and Dirlam 2011), bulk analytical techniques are not quite appropriate. Therefore, it would be beneficial to have a quick and easy to perform analytical method with μm-scale spatial resolution that does not need extensive sample preparation to identify tourmaline species. For a variety of reasons Raman spectroscopy is the method of choice and has been used to systematically study chemical changes in other mineral groups, e.g., feldspars (Mernagh 1991), garnets (Hofmeister and Chopelas 1991), pyroxenes (Wang

et al. 2001), and amphiboles (Leißner et al. 2015). First, the set of Raman-active modes is restricted by symmetry-related selection rules, i.e., the Raman spectrum can be regarded as a fingerprint of a specific tourmaline species. Second, the positions of the Raman peaks and their integrated intensities are related to the compositional site occupancy as the phonon wavenumbers depend on the masses and interatomic force constants of the atoms involved in the corresponding modes, while the relative intensities depend on the abundance of the distinct chemical species. Third, Raman spectroscopy is a non-destructive micrometer-scale technique with no special sample preparation requirements.

In general, there are two approaches to study the chemical composition of the non-tetrahedrally coordinated sites in tourmaline by Raman spectroscopy: by analyzing directly the vibrations related to X-, Y-, and Z-site cations or by analyzing the influence of these cations on the vibrations of the other structural units: the silicate rings and the borate and hydroxyl groups. The O–H bond stretching is a high-energy vibrational mode that is usually observed in the wavenumber range ~3300-3800 cm^{-1}. Therefore, even subtle relative changes in the mode wavenumber due to minor chemical changes in the O–H bond surrounding should result in absolute changes in the peak positions that are large enough to be detected. Thus, the stretching modes of the OH groups in the V and W sites are good candidates for establishing the functional relationship between Raman peak parameters and the crystal chemistry of tourmaline. This approach has been already successfully applied to another mineral supergroup of hydrous complex silicates: amphiboles (Leißner et al. 2015).m

Given the major interest and geological importance of tourmaline, so far relatively few studies have used infrared and/or Raman spectroscopy to analyze different tourmaline species with respect to their chemical composition (e.g., Alvarez and Coy-Yll 1977; Gonzalez-Carreño et al. 1988; Grice and Ercit 1993; Mihailova et al. 1996; Gasharova et al. 1997; Castañeda et al. 2000; Oliveira et al. 2002; McKeown 2008; Hoang et al. 2011; Skogby et al. 2012; Zhao et al. 2012; Fantini et al. 2014; Bosi et al. 2015a,b; Berryman et al. 2015). The infrared studies focus predominantly on the OH bond stretching modes, whereas most of the Raman studies consider the framework vibrations below 1500 cm^{-1} to distinguish between tourmaline species on the chemical joins of, e.g., elbaite-schorl, dravite-buergerite-uvite, buergerite-schorl, uvite-feruvite, elbaite, and fluor-liddicoatite. Hoang et al. (2011) have used the

120 characteristic shape of the Raman spectrum of the O–H bond stretching modes to distinguish four different
121 species, fluor-liddicoatite, elbaite, uvite, and feruvite, and have assigned the observed modes following the
122 model from the infrared studies by Gonzalez-Carreño et al. (1988) and Castañeda et al. (2000). Skogby et
123 al. (2012) considered the OH stretching modes in a single elbaite sample that has been previously
124 characterized by electron and ion microprobe analyses, and structure refinements to X-ray diffraction data.
125 They investigated short-range chemical ordering related to the OH groups and assigned specific local cation
126 arrangements to the V and W site. Fantini et al (2014) investigated five different tourmaline species and
127 assigned different local arrangements based on ion substitution to the two anionic sites. Berryman et al.
128 (2015) studied synthetic tourmalines of four different species and suggested assignments for the different
129 OH-stretching vibrations. However, a detailed Raman-scattering study of the OH stretching range with a
130 number of samples from different tourmaline subgroups and complex chemistry as well as a comprehensive
131 assignment model for the observed OH stretching modes is still missing.

132 Therefore, the objective of this study is to analyze the Raman scattering, in particular arising from
133 the OH stretching modes, of a large variety of natural tourmalines covering the main subgroups of all three
134 primary groups in order to explore the potential of Raman spectroscopy to be used for non-destructive
135 crystallochemical analysis of tourmaline.

136

137 ## MATERIALS AND METHODS

138

139 ### Samples

140 Forty-six natural tourmaline samples from worldwide localities from all three primary tourmaline
141 groups have been studied here, including five alkali subgroups, three calcic subgroups, and two X-vacant
142 subgroups (Table 1). Most of the samples are from the collection of the Mineralogical Museum, Centrum
143 für Naturkunde (CeNak), University of Hamburg, sample S43 was provided by Dr. D. Nishio-Hamane,
144 sample S37 was provided by Dr. E. Lopatka, samples S5, S16, and S35 were provided by Dr. C. Schmidt,
145 and samples S4, S27, S28, S29, S41, and S42 were provided by J. Clanin. The localities of the samples are
146 specified in the supplementary material (Table S1).

147

148 **Raman spectroscopy**

149 Raman scattering experiments were conducted in backscattering geometry with a Horiba Jobin-
150 Yvon T64000 triple-monochromator spectrometer (holographic gratings of 1800 grooves/mm) equipped
151 with an Olympus BX41 confocal microscope (Olympus LM Plan FLN 50x objective with a numerical
152 aperture of 0.5) and a Symphony liquid-N_2-cooled charge-coupled device detector. Raman spectra of all
153 samples were excited by the 514.5-nm line of a Coherent 90C Fred Ar^+ plasma laser. In the case of a high
154 continuum photoluminescence background, additional Raman spectra were collected using a wavelength of
155 488.0 nm. For both laser lines the laser power on the sample surface was approximately 14 mW, which was
156 verified not to generate any sample overheating during the experiment. The achieved spectral resolution
157 was ~2 cm^{-1} and the accuracy in determining the peak positions was ~0.35 cm^{-1}. The spectrometer was
158 calibrated to the silicon Raman peak at 520.5 cm^{-1}.

159 For all samples polarized Raman spectra were collected from raw crystal surfaces in the spectral
160 range 15 – 4000 cm^{-1} in $\bar{y}(zz)y$, $\bar{y}(zx)y$, and $\bar{y}(xx)y$ scattering geometry (Porto's notation); *x*, *y*, and *z*
161 are the Cartesian coordinate axes with *z* parallel to the crystallographic *c* axis in the hexagonal setting,
162 while the crystallographic *a* axis is either along *x* or along *y*. Note that for uniaxial crystals the magnitude
163 of the Raman polarizability tensor components is not changed upon rotation about the *c* axis at 90°, i.e.,
164 both scattering geometries ($a \parallel x$ or $a \parallel y$) generate the same spectra. The acquisition time was chosen to
165 yield a satisfactory signal-to-noise ratio, i.e., most of the spectra were collected for 20 s averaging over 10
166 accumulations. The OriginPro® 9.1 software package was used for data evaluation. The collected spectra
167 were baseline corrected with a spline function, temperature reduced to account for the Bose-Einstein
168 occupation factor $I_{reduced} = I_{measured} /(n(\omega,T)+1)$, $n(\omega,T) = 1/(\exp(\hbar\omega/kT)-1)$ (Kuzmany
169 2009), and normalized to the acquisition time. Peak positions, full widths at half maximum (FWHMs), and
170 integrated intensities were determined from fits with pseudo-Voigt functions
171 $PV = q*Lorentz+(1-q)*Gauss$ with $q \in [0,1]$. The criterion for the maximum number of
172 pseudo-Voigt functions used to simulate the spectrum profile was $\Delta I < I/2$ for all peaks, where *I* and ΔI are
173 the calculated magnitude and uncertainty of the peak intensities.

174

175 **Electron microprobe analysis (EMPA)**

176 Polished specimens were analyzed using a Cameca SX-100 SEM system with a wavelength-
177 dispersive detector. The energy of the electron beam was 15 keV and the beam current was 20 nA. The
178 following standards were used: LiF for F, albite for Na, MgO for Mg, Al_2O_3 for Al, andradite for Si, Ca,
179 and Fe, vanadinite for Cl and V, orthoclase for K, $MnTiO_3$ for Ti and Mn, Cr_3O_3 for Cr, olivinite for Cu,
180 $SrTiO_3$ for Sr, and Ba-glass for Ba. The acquisition times were 20 s for Na, K, Mg, Ca, Mn, Fe, Al, Ti, and
181 Si, 60 s for Ba, Sr, Cu, Cr, and Cl, and 120 s for F. For each element the signal-to-noise ratio was
182 determined by background measurements that were carried out by slight offsetting of the microprobe
183 spectrometer to each side of the X-ray emission peak, measuring a half of the counting time of the
184 corresponding element and obtaining the intensity beneath the emission peak by interpolation. The program
185 WinTcac (Yavuz et al. 2014) was used to calculate the chemical formulae and also for the classification of
186 the tourmaline species, which was additionally verified by the spreadsheet in the supplement of Henry et al.
187 (2011). Since 25 to 50 points were measured for each sample to identify possible chemical variability, the
188 statistical standard deviations allow for a composition precision of about 0.01 atoms per formula unit (apfu)
189 for each element in the calculated chemical formulae.

190

191 **Laser-ablation inductively-coupled-plasma mass spectrometry (LA ICP-MS)**

192 To verify the chemical formulae calculated from EMPA, LA ICP-MS measurements were
193 conducted on selected samples to determine the contents of the light elements B and Li along with Na, K,
194 Ca, Mg, Mn, Fe, Al, Si, and Ti. The experiments were conducted in a He flushed cell with a volume of 35
195 cm^3, using a ThermoFisher Finnigan Element XR high resolution multicollector ICP mass spectrometer
196 connected to an in-house-built laser ablation system based on a Spectra-Physics Solstice femtosecond laser
197 operating with a laser wavelength of 194 nm. Details on the experimental set up are given by Horn et al.
198 (2006) and Oeser et al. (2015). For each sample data were collected from three spatial regions sized
199 approximately 30×30 μm. Each region was subjected to a raster analysis with an ablation spot diameter of

35 μm. The NIST610 glass was used as a calibration standard for all elements. Oxide concentrations were calculated using the program ICPMSDataCal (Liu et al. 2008).

Single-crystal X-ray diffraction

Since the majority of Raman peaks arising from framework phonon modes in sample S33 (povondraite) showed significant downward shifts as compared to the other tourmalines, the tourmaline-type structure of this sample and sample S36 (fluor-buergerite) were double checked by single-crystal X-ray diffraction analysis. The experiments were conducted with a Nonius KappaCCD diffractometer, using graphite monochromated Mo Kα radiation. Pixel intensities were integrated using the Eval15 suite of programs (Schreurs et al. 2010). Structure refinements were performed using the program Jana2006 (Petricek et al. 2014). Scattering factors of uncharged atoms were used throughout. The site occupancies of the Y and Z-sites were refined based on scattering functions for Fe and Mg, assuming that scattering contributions from the minor elements Ti and Al do not deviate significantly from Fe and Mg respectively.

RESULTS AND DISCUSSION

Chemical composition from EMPA and LA ICP-MS

Tourmalines contain typically 10-11 wt% B_2O_3, up to about 3.8 wt% H_2O and variable amounts of Li_2O up to about 3.5 wt%. Thus, the EMPA data points with total oxide sums below 82 wt% were excluded from the subsequent statistic averaging as they may represent analysis of surface defects. The calculations of the chemical formulae followed the procedure for normalization of EMPA data and estimation of light elements described in appendix V by Henry et al. (2011). The anionic sites are assumed to sum up to four, boron is calculated stochiometrically as three boron atoms per formula unit. For tourmalines with assumed low Li content the sum of T+Z+Y cations is normalized to 15, for all other samples normalization was done on the basis of Si = 6. In the case that the content of Li is estimated, this is done on the basis the Li fills any cation deficiency in the Y site. Hydrogen contents are determined by charge balance assuming the oxidation states of iron and manganese to be divalent except for fluor-buergerite (S36) and povondraite (S33), where all iron is trivalent. The total oxide sums amount to 99.7 ± 2.7 wt% for all samples when the

amounts of non-measured light elements are included. The chemistry of all fourty-six tourmaline samples and their classification according to the 2011 IMA tourmaline-supergroup nomenclature is given in Table 1. The raw EMPA data are given in Supplementary Table S2.

In addition, the amounts of lithium and boron were experimentally determined by LA ICP-MS measurements. Figure 2 compares the measured and calculated contents of B_2O_3 and Li_2O for certain samples, which are in reasonably good agreement. The small deviations from the ideal one-to-one correlation, in particular for Li, all fall in the range of 0.1-0.3 apfu, which is the precision of the estimation of Li (Henry et al. 2011). As stated by Henry et al (2011), Li contents calculated from EMP data tend to be underestimated, which can also be seen in Fig. 2. Small deviations are also possible due to slight spatial divergences of the measurement spots of LA ICP-MS and EMPA, though backscattered electron images from the microprobe analysis spots were used to determine the positions for the LA ICP-MS and Raman measurements. In the following discussion, we use the contents of Li and B calculated from EMPA data.

Raman-scattering analysis

Group-theory considerations. Site symmetry group-theory analysis (Kroumova et al. 2003) predicts $32A_1 + 22A_2 + 54E$ phonon modes in tourmalines, one $A_1 + E$ of which are acoustic and the rest, $31A_1 + 22A_2 + 53E$, are optical. The acoustic modes are the lowest-energy phonon modes and therefore they are associated with the atoms having the largest mass and/or participating in the weakest interactions. In tourmalines such atoms are the X-site cations. The A_1 and E optical modes are simultaneously Raman- and infrared-active, while the A_2 modes are inactive. Thus, 31 peaks generated by A_1 modes should be observed in $\bar{y}(zz)y$ spectra, 53 peaks generated by E modes should appear in $\bar{y}(zx)y$ spectra, and all 84 optical phonon modes contribute to the $\bar{y}(xx)y$ spectra (Table 2). However, less Raman peaks may be experimentally observed because of too low intensities of certain phonon vibrations and/or peak overlap. As an example, Fig. 3 shows a set of polarized Raman spectra of dravite measured in all possible scattering geometries. As can be seen, the peak intensity strongly depends on the scattering geometry. Furthermore, since 3*m* is a polar crystal class, the positions of peaks arising from the longitudinal optical (LO) A_1 and E modes may be higher than the positions of peaks arising from the corresponding transverse optical (TO) A_1

and E modes. Therefore, when chemically induced changes in the Raman peaks are analyzed, all samples should be measured in the same scattering geometry. In this study, we focused our analysis on $\bar{y}(zz)y$ spectra, in which the Raman intensities of the OH-stretching phonon modes are strongest. According to the site symmetry analysis, H(1) atoms (belonging to the ^{W}OH groups) participate in A_1 + E Raman-active modes, whereas H(3) atoms (belonging to the ^{V}OH groups) participate in $2A_1$ + 3E modes (see Table 2). Symmetry considerations of the atomic vector displacements comprising the phonon modes (Kroumova et al. 2003) reveal that the ^{W}OH groups exhibit one O–H bond stretching vibration along the *c* axis (A_1 mode) and one O–H bond libration (E mode) within the (*a*,*b*) plane. The ^{V}OH groups generate two A_1 modes: one stretching mode along the *c* axis and one libration mode within the (*a,b*) plane as well as three E modes: one stretching vibration along the *c* axis and two libration modes within the (*a*,*b*) plane. Therefore, polarized $\bar{y}(zz)y$ Raman spectra of tourmalines with no chemical deviation from the end-member composition should contain only two peaks in the spectral range 3300–3900 cm^{-1}: one arising from an A_1-type ^{W}OH stretching and one from an A_1-type ^{V}OH stretching mode. However, as can be seen in Fig. 4, this is obviously not the case. All tourmaline spectra studied here and in general the spectra of tourmaline species reported in the literature so far exhibit a complex shape of several, partially overlapping peaks. The significant deviation from the expected number of only two OH-stretching peaks is due the existence of diverse chemical species surrounding the hydroxyl groups, when one or more crystallographic cationic sites are occupied by at least two different elements.

OH stretching mode assignment model. The O-H bonding is very sensitive to its local atomic surrounding. The wide variety of incorporated elements allows for a large number of possible substitutions (Hawthorne 1996), in particular on the X and Y site, but also on the Z and T site. The mode-assignment model presented here assumes that the ^{V}OH vibrations are primarily affected by the chemistry of the three YZZ octahedral triplets sharing the O(3) atom with the ^{V}OH group (see Fig. 1), whereas the ^{W}OH vibrations are strongly influenced by both the YYY octahedral triplet sharing the O(1) atom with ^{W}OH and the X-site cation next to the $^{W}H^{+}$ cation. Thus, the diversity of the local chemical environments of the W site as well as of the three symmetry-equivalent V sites per formula unit causes the increased number of OH-stretching peaks (see Fig. 4) due to two-mode behavior (Chang and Mitra 1971). It should be

emphasized that three V-site H cations participate in a single phonon mode and therefore one has to consider the atomic surrounding of all three H(3) atoms in the primitive unit cell, i.e. the wavenumber of the ^{V}OH stretching mode depends on the chemistry of the YZZ-YZZ-YZZ configuration, not on the chemistry of a sole YZZ species. Secondary effects on the OH modes by longer-distanced cations are expected to cause composition-induced shifts in the peaks positions due to one-mode behavior (Chang and Mitra 1971).

Our assignment model is based on the following arguments: (i) ^{V}OH and ^{W}OH stretching modes can be distinguished by their frequencies and relative intensities. Raman peaks above ~3615 cm^{-1} originate from vibrations of the ^{W}OH group as the O(1)–H(1) bond length is in general shorter and thus weaker than the O(3)–H(3) bond length, so that ^{V}OH stretching modes can be observed from about 3400–3615 cm^{-1} (Gonzalez-Carreño et al. 1988; Castañeda et al. 2002; Bosi et al. 2012; Gatta et al. 2014). (ii) An inverse correlation of the mode wavenumber with the sum of the charges of the three octahedral cations, which coordinate the OH group, is expected (Gonzalez-Carreño et al. 1988; Martìnez-Alonso et al. 2002). Higher octahedral cationic charges strengthen the cation-oxygen bond so that the O–H bond strength effectively decreases and consequently the OH stretching mode shifts towards lower wavenumbers. (iii) There is a strong influence of the occupancy of the X site on wavenumber of the ^{W}OH stretching modes, whereas it is minor on the ^{V}OH modes due to the longer distance between the V and X site. A positively charged cation occupying the X site repulsively interacts with the H^{+} cation of the ^{W}OH group creating an effective confined space of motion for the O-H bond stretching (Gonzalez-Carreño et al. 1988; Leißner et al. 2015). Thus, ^{W}OH stretching modes associated with $^{X}\square$ appear at ~3615–3685 cm^{-1}, whereas modes associated with occupied X sites at ~3710–3820 cm^{-1} and among these the order from lower to higher wavenumber is ^{X}Na, ^{X}Ca, ^{X}K due to cationic charge and size (Berryman et al. 2015).

^{V}OH stretching mode assignment for different tourmaline species. The arguments given above lead to the following ^{V}OH stretching mode assignments of the tourmaline species in this study. For all alkali tourmaline species the most intense ^{V}OH peaks are assigned to the most probable YZZ-YZZ-YZZ triplet occupancy corresponding to the end-member composition. Thus, in dravite (Fig. 5a), the most intense ^{V}OH mode (3573±4 cm^{-1}, Table 3) is assigned to $3^{Y}Mg^{Z}Al^{Z}Al$, representing the composition of the

ordered end member, even if there is a certain amount of Y-/Z-site occupancy disorder of Mg and Al (Hawthorne et al. 1993). Aluminum is the most common substituent in dravite and therefore, when the amount of octahedral Al increases, the YZZ triplets are overcharged compared to the chemical species corresponding to the end-member composition. Consequently, the ^{V}OH-stretching modes corresponding to $2^{Y}Mg^{Z}Al^{Z}Al$-$^{Y}Al^{Z}Al^{Z}Al$ and $^{Y}Mg^{Z}Al^{Z}Al$-$2^{Y}Al^{Z}Al^{Z}Al$ appear at lower wavenumbers, 3534±7 and 3494±8 cm^{-1}, as compared to the dominant mode.

The mode assignment for the ^{V}OH modes in schorl is analogous to that of dravite, but with $^{Y}Fe^{2+}$ instead ^{Y}Mg (Fig. 5c). The peaks appear systematically at lower wavenumbers than the corresponding ones in dravite (see Table 3) due to the stronger Fe^{2+}-O interaction as compared to Mg-O interaction. A similar downwards wavenumber shift depending on the Fe^{2+}/Mg content is observed in amphiboles (Leißner et al. 2015).

For elbaite, the two dominant ^{V}OH modes are likewise related to the most probable YZZ triplets: the peak at 3593±4 cm^{-1} is associated with $2^{Y}Li^{Z}Al^{Z}Al$-$^{Y}Al^{Z}Al^{Z}Al$ and that at 3494±8 cm^{-1} with $^{Y}Li^{Z}Al^{Z}Al$-$2^{Y}Al^{Z}Al^{Z}Al$ (Fig. 5e). In addition, modes related to the major substituent $^{Y}(Fe^{2+}, Mn^{2+})$ can often be observed with their intensity related to the element content. The mode at 3562±4 cm^{-1} is assigned to $2^{Y}Fe^{*Z}Al^{Z}Al$-$^{Y}Al^{Z}Al^{Z}Al$ and the one at 3465±11 cm^{-1} to $^{Y}Fe^{*Z}Al^{Z}Al$-$2^{Y}Al^{Z}Al^{Z}Al$ with $^{Y}Fe^{*}=(^{Y}Fe^{2+}+^{Y}Mn^{2+})$. Separate Raman peaks exclusively related to either divalent iron or manganese cannot be distinguished, because these elements are very similar in mass, electronegativity, and ionic radius, which thus results in almost the same vibrational frequencies. The same ^{V}OH mode assignment is also used for darrellhenryite (samples S34 and S35) as this species should contain the same type of YZZ-YZZ and YYY-X chemical species as elbaite. Indeed experimentally no differences in the OH-peak positions within the errors are observed for Fe*-low elbaite and darrellhenryite samples.

Povondraite is an alkali, ferri iron-containing tourmaline species, which contains no Al, but ferric iron and magnesium on the Z site. For short-range bond-valence requirements, the W site is solely occupied by oxygen. The Raman spectrum in Fig. 4 supports this site occupancy and the two observed ^{V}OH stretching vibrations at 3554±1 cm^{-1} and 3596±2 cm^{-1} are attributed to $2^{Y}(Fe^{3+})^{Z}(Fe^{3+})^{Z}Mg$-$^{Y}(Fe^{3+})^{Z}(Fe^{3+})^{Z}(Fe^{3+})$ and $3^{Y}(Fe^{3+})^{Z}(Fe^{3+})^{Z}Mg$, respectively. X-ray single crystal structure refinement of

335 povondraite confirms the predominantly trivalent state of Fe, as indicated by the bond valence sums at both
336 the Y and Z sites (Supplementary table 4). Judging by the averaged bond distances of these sites, Fe^{2+}
337 would be strongly overbonded with a BVS of 2.58 and 2.82 respectively. The W site is significantly
338 underbonded, with a BVS of 1.64. This underbonding would be even larger if not the entire Ti^{4+}-content
339 obtained by EMPA would be attributed to the Y-site. It can thus be concluded that the 0.59 apfu Ti mainly
340 occupy the Y site, where they substitute for Fe^{3+}. All other BVS are reasonably close to the formal charges
341 of the cations and anions that constitute povondraite. Al has been attributed to the Z site, because it would
342 be even more strongly underbonded at the Y site. With the addition of Al and Ti from EMPA, the
343 povondraite formula obtained by X-ray structure refinement is
344 $Na_{0.63}K_{0.37}(Fe^{3+}_{1.64}Mg_{0.77}Ti_{0.59})(Fe^{3+}_{3.97}Mg_{1.57}Al_{0.47})(BO_3)_3Si_6O_{18}(OH)_3O$, which amounts to a slightly
345 increased Mg/Fe^{3+} ratio, when compared with the EMPA (Table 1), but is otherwise in good agreement
346 with the latter. The slight excess of 0.28 positive charges in the chemical formula might suggest that
347 approximately 0.2 Fe^{2+} apfu substitute for Fe^{3+}, i.e. approximately 3.5 % of Fe might be divalent. V-site H
348 forms a weak hydrogen bond with O5 (O5-H3 bond valence of 0.053 vu), in accordance with the hydrogen
349 bonding in oxy-dravite determined by Gatta et al. (2014).

350 In fluor-buergerite and olenite the V site is nominally fully occupied by O^{2-}, which implies that the
351 Raman peak associated with ^{V}OH should be absent in the spectra. However, even though the OH stretching
352 modes of these two species have significantly lower intensities compared to the tourmaline species
353 discussed above, both spectra clearly show OH stretching modes in the wavenumber range of the ^{V}OH
354 groups (Fig. 4). In agreement with Bosi et al. (2015a), this is attributed to occupancy disorder of OH over
355 both V and W sites. Therefore, the ^{V}OH modes in fluor-buergerite are assigned to $3^{Y}(Fe^{3+})^{Z}Al^{Z}Al$ (3531±1
356 cm^{-1}) and $2^{Y}(Fe^{3+})^{Z}Al^{Z}Al$-$^{Y}Al^{Z}Al^{Z}Al$ (3490±2 cm^{-1}) (Table 3). Possible small amounts of divalent iron
357 (Donnay et al. 1996) might result in the occurrence of a peak related to $3^{Y}(Fe^{2+})^{Z}Al^{Z}Al$ at about 3573±3 cm^{-1}. It should be noted that there is a considerable downshift of the Fe^{3+}-related ^{V}OH stretching modes
359 compared to their Fe^{2+}-related analogous modes in schorl. The dominant ^{V}OH peak in fluor-buergerite is
360 ~35 cm^{-1} lower than that in schorl, so the two species can be immediately discriminated, but the

361 determination of plausible Fe^{3+} in schorl is hindered by the overlap with ^{V}OH peaks resulting from ^{Y}Al-rich
362 species.

363 The dominant ^{V}OH stretching mode in olenite appears at 3455±1 cm^{-1} and it is assigned to
364 $3^{Y}Al^{Z}Al^{Z}Al$ (Table 3). Additionally, the spectrum shows a peak at 3592±1 cm^{-1} attributed to $2^{Y}Li^{Z}Al^{Z}Al$-
365 $^{Y}Al^{Z}Al^{Z}Al$ due to the perfect match with the position of the corresponding peak in elbaite, a weak peak at
366 3562±7 cm^{-1} that is associated with $2^{Y}Fe^{*Z}Al^{Z}Al$-$^{Y}Al^{Z}Al^{Z}Al$, and a broad peak at 3504±4 cm^{-1} that may be
367 attributed to either $^{Y}Li^{Z}Al^{Z}Al$-$2^{Y}Al^{Z}Al^{Z}Al$ or $^{Y}Fe^{*Z}Al^{Z}Al$-$2^{Y}Al^{Z}Al^{Z}Al$ or to the coexistence of both
368 chemical species. EMPA calculations indicate none or too little Li in this sample, depending on the Li-
369 estimation procedure (Henry et al. 2011). Hence, the occurrence of Li-related ^{V}OH and also ^{W}OH modes in
370 the spectrum of our olenite sample is most probably due to a slight mismatch in the spatial regions
371 measured by EMPA and Raman spectroscopy. Samples from this locality (Olenii Ridge, Kola Peninsula,
372 Russia, Supplementary Table S1) are known to have elbaite cores and olenite rims. Thus, the Li-related
373 vibrations originate from the intergrowth of the elbaite fraction of the sample.

374 The ^{V}OH mode assignment for tourmalines from the calcic subgroup is slightly different from that
375 for the alkali subgroup as the dominant ^{V}OH stretching is not related to the YZZ-YZZ-YZZ species
376 expected from the chemical composition of the ordered end member. This is due to the higher charge of
377 calcium (2+) compared to sodium (1+). For example, in uvite Mg and Al can be almost randomly
378 distributed over both Y and Z sites in accordance to previous studies (Hawthorne 1996). Indeed, the
379 presence of ^{Y}Al can be deduced from the occurrence of the same ^{W}OH stretching modes as in dravite (see
380 Fig. 5 and Table 3). Therefore, the ^{V}OH modes are assigned only to distinguished chemical octahedral
381 triplets, without specifying the cationic site allocations. However, the cationic chemical species can still be
382 inferred from the arguments regarding the charge of the octahedral cations, starting from the lowest-
383 wavenumber peak. The latter should be related to the most strongly overcharged YZZ-YZZ-YZZ species,
384 i.e. Al-richest species. In uvite, this should correspond to 3MgAlAl, because further Al substitution for Mg
385 would correspond to dravite species. Thus, we assign the uvite lowest-wavenumber ^{V}OH-stretching peak at
386 3485±5 cm^{-1} to 3MgAlAl. This peak appears at much lower wavenumber than the ^{V}OH-MgAlAl peak in
387 dravite most probably because in uvite the 3MgAlAl species are entirely associated with X-site vacancies,

388 while in dravite they are in the vicinity of filled X sites (see the discussion in subsection **Wavenumbers of**
389 **the ^{V}OH stretching modes**). By gradual substitution of Mg for Al, the ^{V}OH peaks at higher wavenumbers
390 are then attributed to MgAlAl-2MgMgAl (3518±3 cm^{-1}), 2MgMgAl-MgAlAl (3547±2 cm^{-1}), and
391 3MgMgAl (3579±2 cm^{-1}) (Fig. 5b). The enhanced undercharge of the YZZ triplets as well as the increased
392 average ionic radius ($r_i(Mg^{2+}) > r_i(Al^{3+})$) are compensated by the higher-charged Ca^{2+} in the close-by X
393 sites, which in nine-fold coordination has an ionic radius smaller than that of Na^{+} (Shannon 1976).
394 Moreover, this assignment is also supported by the inverse correlation between the sum of octahedral
395 cationic radii and the mode frequency as all uvite modes are shifted to higher wavenumbers compared to
396 dravite (Table 3 and Fig. 6a).

397 The assignment of the dominant ^{V}OH mode in fluor-liddicoatite to $3^{Y}Li^{Z}Al^{Z}Al$ instead of
398 $2^{Y}Li^{Z}Al^{Z}Al$-$^{Y}Al^{Z}Al^{Z}Al$, representing the end-member stoichiometry, is comparable to the assignment of the
399 dominant mode in uvite. The additional modes in descending order are assigned to $2^{Y}Li^{Z}Al^{Z}Al$-$^{Y}Al^{Z}Al^{Z}Al$
400 (3582±3 cm^{-1}), $^{Y}Li^{Z}Al^{Z}Al$-$^{Y}Fe^{*Z}Al^{Z}Al$-$^{Y}Al^{Z}Al^{Z}Al$ (3551±6 cm^{-1}), $^{Y}Li^{Z}Al^{Z}Al$-$2^{Y}Al^{Z}Al^{Z}Al$ (3511±3 cm^{-1}),
401 and $3^{Y}Al^{Z}Al^{Z}Al$ (3475±7 cm^{-1}) (Table 3).

402 Adachiite is a special, recently recognized, tourmaline species containing Al on the T site (Nishio-
403 Hamane et al. 2014). Although it belongs to the calcic group, $3^{Y}Fe^{Z}Al^{Z}Al$ with nominally overcharged YZZ
404 triplet occupancies is the dominant ^{V}OH stretching mode (see Table 3). This overcharge is compensated by
405 the substitution of ^{T}Al for ^{T}Si in the tetrahedral ring, which also accounts for the shift towards lower
406 wavenumbers of all modes compared to their analogous species in tourmalines with six ^{T}Si per formula
407 unit. The difference of about 30 cm^{-1} of the ^{V}OH stretching related to $3^{Y}Fe^{Z}Al^{Z}Al$ between adachiite and
408 schorl is in agreement with similar ^{T}Al-induced downward frequency shifts observed in amphiboles and
409 micas (Hawthorne et al. 1996).

410 The assignment of the OH stretching modes of species of the X-vacant subgroup follows the same
411 logic as for the alkali subgroup. The difference is that the most probable YZZ-YZZ-YZZ species is
412 overcharged as compared to the alkali subgroup, which is compensated by the prevalence of X-site
413 vacancies. Thus, the most intense ^{V}OH-stretching peak in foitite at 3551±1 cm^{-1} is related to $2^{Y}Fe^{*Z}Al^{Z}Al$-
414 $^{Y}Al^{Z}Al^{Z}Al$ (Fig. 5d) with Fe* = Fe^{2+}, which matches the end-member formula. The presence of X-site

cations can be structurally balanced by lower-charged YZZ triplets so that a shoulder at higher wavenumbers (3566±1 cm^{-1}) is observed, which is assigned to $3^{Y}Fe^{*Z}Al^{Z}Al$. This assignment is strongly supported by the fact that the position of this extra Raman scattering in the spectrum of foitite matches well the position of the main peak in schorl spectra. The other well pronounced ^{V}OH peak in the spectrum of foitite appears at a lower wavenumber (3484±6 cm^{-1}) than the strongest ^{V}OH peak and thus it is assigned to an even more overcharged YZZ-YZZ-YZZ configuration: $^{Y}Fe^{*Z}Al^{Z}Al\text{-}2^{Y}Al^{Z}Al^{Z}Al$. For ^{Y}Li-containing foitites, an additional peak at 3517±2 cm^{-1} can be observed, which is assigned to $^{Y}Li^{Z}Al^{Z}Al\text{-}2^{Y}Al^{Z}Al^{Z}Al$ (Fig. 5d). This assignment is also used for sample S46, the □-Fe-O root name species, as its Raman spectrum shows no significant differences to the spectra of foitite.

^{W}OH stretching mode assignment for different tourmaline species. As explained above, the assignment of the ^{W}OH stretching modes is based on the chemistry of YYY-X configurations. The majority of tourmaline species studied here exhibit Raman peaks in the range 3615-3685 cm^{-1}, which are caused by the stretching of ^{W}OH groups next to vacant X sites, whereas ^{W}OH modes related to filled X sites (3710-3810 cm^{-1}) are only observed, if the total OH content is larger than ~3.3 apfu (see Table 1). This is a strong indication that ^{W}OH groups prefer to be situated next to vacant X sites.

Our assignment of the Raman peaks arising from ^{W}OH groups next to filled X sites takes only stable YYY clusters of mono-, di-, and trivalent cations into account, obeying the short-range bond-valence requirements at the O(1) site (Bosi et al. 2013). However, the assignment of the ^{W}OH stretching modes related to ^{X}□ includes also overcharged YYY species that are not favored by bond-valence-theory considerations. The reason is that to obey the short-range bond-valence requirements overcharged YYY triples have been so far as associated with O^{2-} on the W site. However, a vacancy on the X site next to a given ^{W}OH group can promote an overcharged YYY species in the vicinity of the same ^{W}OH group, i.e., the charge compensation of the species YYY-W-X can be realized by locally coupled overcharged YYY species and a vacant X site, rather than by O^{2-} on the W site. This extends the possible YYY configurations associated with ^{W}OH groups next to vacant X sites and complicates the peak assignment. So, below we will consider first the Raman peaks attributed to YYY-^{W}OH-^{X}□ for all tourmaline species, starting with foitite as representative for the X-vacant subgroup. Then, we will assign the Raman peaks attributed to YYY-

442 ^{W}OH- X_{filled} for all tourmaline species, starting with the dravite samples because they exhibit the highest
443 amount of OH apfu among all the samples studied here.

444 Foitite is characterized by two strong ^{W}OH-stretching peaks at 3631±1 and 3644±1 cm^{-1} related to
445 YYY-^{W}OH-^{X}□. The two peaks can be assigned either to ^{Y}Fe*^{Y}Fe*^{Y}Al–^{X}□ and ^{Y}Fe*^{Y}Fe*^{Y}Fe*–^{X}□
446 configurations or to ^{Y}Fe*^{Y}Al^{Y}Al–^{X}□ and ^{Y}Fe*^{Y}Fe*^{Y}Al–^{X}□ configurations. The former is consistent with
447 stable YYY species given by bond-valence analyses, but the latter matches the YYY species deduced from
448 the two dominant ^{V}OH-stretching peaks at 3384±6 and 3551±1 cm^{-1}. Moreover, if the first assignment
449 would be valid, it would indicate oddly large amount of ^{Y}Fe*^{Y}Fe*^{Y}Fe*-^{W}OH-^{X}□ species, which are
450 undercharged and untypical of foitite. Hence, we assign the ^{W}OH-stretching peaks at 3631±1 and 3644±1
451 cm^{-1} to ^{Y}Fe*^{Y}Al^{Y}Al–^{X}□ and ^{Y}Fe*^{Y}Fe*^{Y}Al–^{X}□ species, respectively. Schorl samples studied here exhibit
452 one ^{W}OH-stretching peak at 3630±1 cm^{-1} related to YYY-^{X}□ species, which matches perfectly the position
453 of the ^{Y}Fe*^{Y}Al^{Y}Al-^{W}OH-^{X}□ peak in foitite and thus it is assigned to ^{Y}Fe*^{Y}Al^{Y}Al-^{X}□ (see Table 3). Both
454 dravite and uvite have two ^{W}OH-stretching peaks at 3639±3 and 3668±3 cm^{-1} related to YYY-^{X}□ species.
455 The two peaks are slightly shifted towards higher wavenumbers as compared to the corresponding peaks in
456 foitite and hence they are assigned to ^{Y}Mg^{Y}Al^{Y}Al-^{X}□ and ^{Y}Mg^{Y}Mg^{Y}Al-^{X}□. It has to be emphasized that
457 dravite and uvite generate ^{W}OH peaks at exactly the same positions (see Table 3 and Fig. 5), revealing
458 identical chemical YYY-^{X}□ species and underlining the occurrence of Y-/Z-site occupancy disorder.
459 Elbaite, darrellhenryite, fluor-liddicoaitite, and olenite studied here show a peak at 3652±3 cm^{-1}, which is
460 assigned to ^{Y}Li^{Y}Al^{Y}Al-^{X}□. (Fe^{2+},Mn)-containing elbaite exhibits a peak at 3678±4 cm^{-1}, which is attributed
461 to ^{Y}Li^{Y}(Li,Fe*)^{Y}Al-^{X}□ species. A weak peak at 3670±1 cm^{-1} is observed in Li-bearing foitites and hence
462 may indicate ^{Y}Li^{Y}Fe*^{Y}Al–^{X}□ species. The validity of the peak assignments for all considered tourmaline
463 species is strengthened by the fact that the position of the ^{Y}R^{Y}Al^{Y}Al-^{W}OH-^{X}□ as well as of the ^{Y}R^{Y}R^{Y}Al-
464 ^{W}OH-^{X}□ peak increases in the order ^{Y}R = ^{Y}Fe* → ^{Y}Mg → ^{Y}Li. The only exception is adachiite, showing a
465 peak at 3625±1 cm^{-1}. The peak is assigned to ^{Y}Fe^{Y}Fe^{Y}Al–^{X}□ and the significant wavenumber downshift as
466 compared to the corresponding peak for foitite is ascribed to the presence of ^{T}Al.

467 Dravite and uvite samples show two peaks related to YYY-^{W}OH-X_{filled}: at 3740±4 and 3770±2 cm^{-}
468 ^{1}. Again the positions of the peaks are the same within uncertainties for both tourmaline species, indicating

the same YYY-X_{filled} species. The two peaks can originate from two different YYY species associated with the same type of X-site cation or from the same YYY species associated with two different types of X-site cations. The chemical compositions of the natural dravite and uvite samples studied here allows for the latter interpretation. However synthetic K-dravite also shows two ^{W}OH peaks related to filled X site (Berryman et al. 2015), which indicates these two peaks should be attributed to two different YYY species. In addition, our preliminary temperature-dependent Raman measurements indicate that the peak near 3770 cm^{-1} splits in two at low temperatures. Therefore the ^{W}OH peaks at 3740 and 3770 cm^{-1} are assigned to $^{Y}Mg^{Y}Mg^{Y}Al$–^{X}Na and $^{Y}Mg^{Y}Mg^{Y}Mg$–^{X}(Na+Ca), respectively. Schorl and foitite show one ^{W}OH peak around 3723 cm^{-1} related to occupied X sites and it is assigned to $^{Y}Fe^{*Y}Fe^{*Y}Al$–^{X}Na. Elbaite and darrellhenryite exhibit one peak at 3714±2 cm^{-1} and it is attributed to $^{Y}Li^{Y}Al^{Y}Al$–^{X}Na. Possible assignment of this peak to $^{Y}Li^{Y}Li^{Y}Al$–^{X}Na is ruled out, because the $^{Y}R^{Y}R^{Y}Al$–^{X}Na peak position should increase in the order $^{Y}R = {}^{Y}Fe^{*} \rightarrow {}^{Y}Mg \rightarrow {}^{Y}Li$. Again the only exception of this expected trend is the ^{T}Al-containing tourmaline species adachiite, having a peak at 3679±1 cm^{-1} attributed to a combination of $^{Y}Fe^{Y}Fe^{Y}Al$–^{X}Na and $^{Y}Mg^{Y}Mg^{Y}Al$–^{X}Na.

The assignment of the ^{V}OH and ^{W}OH stretching modes is supported by the behavior of the averaged ionic radii of the cations in the trimer of YZZ triplets $\langle r_{YZZ} \rangle$ as well as in the YYY triplet $\langle r_{YYY} \rangle$, calculated from data on ionic radii of the corresponding elements in tourmaline (Bosi and Lucchesi 2007), with the average wavenumbers of the corresponding OH stretching modes (Fig. 6a,b). The mean ionic radius $\langle r_{YZZ} \rangle$ decreases with the increase in the octahedral cation–O(3) (cation-^{V}O) bond strength and therefore, it should positively correlate with the O(3)–H(3) (^{V}O-^{V}H) bond strength and the corresponding peak position. Figure 6a clearly shows such a correlation within the same tourmaline species. Likewise, with the substitution of higher-charged cations on the Y site, $\langle r_{YYY} \rangle$ decreases and so does the ^{W}OH-stretching wavenumber (see Fig. 6b). The effect of the X site on the position of the ^{W}OH modes can be inferred from the same $\langle r_{YYY} \rangle$ value but different averaged positions of $^{Y}Mg^{Y}Mg^{Y}Al$ or $^{Y}Fe^{Y}Fe^{Y}Al$ with $^{X}\square$ and ^{X}Na or ^{X}(Na+Ca) (Fig. 6b).

Integrated intensities of the ^{V}OH stretching modes. Changes in both the X- and Y-site occupancy are more directly reflected by the ^{W}OH vibrational modes than by the ^{V}OH vibrations, because

both the X- and Y-site cations interact directly with the W-site anions, resulting in two-mode behavior of ^{W}OH stretching. However, F^- and O^{2-} anions commonly replace OH^- groups on the W site rather than on the V site (Grice and Ercit 1993; Henry and Dutrow 2011). In addition, our data indicate that if the W site is only partially occupied by OH^- groups, the ^{W}OH are preferably placed next to the vacant X site rather than to be randomly distributed in the vicinity of both vacant and occupied X sites. Consequently, predominantly overcharged YYY species are detected via ^{W}OH vibrations. Therefore, the Raman intensities of the ^{W}OH-stretching peaks do not mirror correctly the X-site and Y-site occupancy. Thus, in the following we focus on the ^{V}OH stretching modes and use the integrated intensities for quantitative determination of the contents of the dominant Y-site elements/major substituents Mg, (Fe^{2+}+Mn^{2+}), Li, and Al.

The content of a Y-site element can be calculated by adding up the integrated intensities of those ^{V}OH peaks to which this element contributes with the corresponding intensity multiplied by the number of occupied Y octahedra by this element in the corresponding YZZ-YZZ-YZZ species. This total sum is normalized to the sum of the integrated intensity of all ^{V}OH modes. For example, the ^{Y}Mg content in dravite can be calculated by

$$^{Y}Mg_{Raman}\,(apfu) = (3I_{3^{Y}Mg^{Z}Al^{Z}Al} + 2I_{2^{Y}Mg^{Z}Al^{Z}Al-{}^{Y}Al^{Z}Al^{Z}Al} + I_{^{Y}Mg^{Z}Al^{Z}Al-2^{Y}Al^{Z}Al^{Z}Al})/I_{^{V}OH_{total}}$$

with I being the integrated intensity of each corresponding Mg-bearing OH stretching mode and $I_{^{V}OH_{total}}$ the sum of the integrated intensities of all ^{V}OH modes. A similar approach was successfully applied to determine the amount of octahedrally coordinated Mg and Fe^{2+} in amphiboles (Leißner et al. 2015). Figures 7a-d show the contents of ^{Y}Mg, ^{Y}(Fe^{2+}+Mn^{2+}), ^{Y}Li, and ^{Y}Al calculated from the integrated intensities of the Raman peaks in comparison to the element contents determined by EMPA. Good agreements along the one-to-one correlation lines within the errors are achieved for all major elements occupying the Y site in tourmalines. Small deviations from the one-to-one correlation lines, particularly for schorl, in Figs. 7a,b may in part results from the possible partial disorder of Mg and Fe^{2+} over the Y and Z site (e.g., Hawthorne et al. 1993; Henry et al. 2011; Bosi et al. 2015b). The calculation of the site occupancies from the EMP data does not account for this and hence the total amounts of measured Mg and Fe are assigned to the Y site so that the ^{Y}Mg and ^{Y}Fe contents might be overestimated. This can particularly be the case for tourmalines

with significant amount of O^{2-} on the W site. The contents calculated from the integrated intensities of the Raman scattering analysis consider only the number of occupied octahedra by a certain element in the YZZ-YZZ-YZZ species, no matter if it is on the Y or Z site. Conveniently, the existence of occupancy disorder is inherently included in the element contents calculated from ^{V}OH Raman peak intensities, which suggests that the latter is not biased by any assumptions about element site distribution and thus better reflects the real crystal chemistry of tourmalines. The small deviations of the data points from the one-to-one correlation lines in Figs. 7c,d maybe due to possible additional substitutions of subtle amounts of other elements whose vibrational modes are not distinguishable from the assigned ones due to overlapping peaks, or possible slight mismatches between the measurement spots of EMP and Raman scattering analysis (e.g., sample S37 as discussed above).

In elbaite, the ^{Y}Fe* (Fe* = Fe^{2+}, Mn^{2+}) impurities strongly affect the integrated intensity of the ^{V}OH-stretching mode arising from ^{Y}Fe*^{Z}Al^{Z}Al-2^{Y}Al^{Z}Al^{Z}Al species, while it does not impact the integrated intensity of the dominant ^{V}OH mode related to ^{Y}Li^{Z}Al^{Z}Al-2^{Y}Al^{Z}Al^{Z}Al species. Thus, the intensity ratio of these two modes is directly correlated with the content of ^{Y}(Fe+Mn) (Fig. 8). The fitted linear equation has a small relative error of 6% so that for tourmaline species which do not nominally contain Fe^{2+} or Mn^{2+} this procedure yields better results in the determined ^{Y}(Fe+Mn) content than that shown in Fig. 7b. An attempt was made to determine the ^{Y}Mn/^{Y}(Fe^{2+} Mn) ratio by considering different intensity ratios as well as shifts in the Raman peak positions, but unfortunately no reliable unambiguous trend was found to discriminate Mn and Fe^{2+}.

Wavenumbers of the ^{V}OH stretching modes. In order to check whether the X-site chemistry can be estimated from the ^{V}OH-stretching peaks, the peak positions for the Mg-, Fe^{*}-, and Li-containing tourmaline species were plotted versus the sum of ^{X}Na and ^{X}Ca contents measured by electron microprobe (see Figs. 9a, 10a, and 11a, respectively). The observed trends reveal association of certain YZZ octahedral configurations with occupied or vacant X sites in their vicinity. In some cases, further preferred relations to either cation can be deduced from the frequency shifts depending on the normalized sodium content (Fig. 9b, 10b, and 11b).

549 The wavenumbers ω of all ^{V}OH modes in dravite show positive trends with the increased number
550 of filled X sites (Fig. 9a). The data points can be fitted with linear functions, but with comparatively large
551 relative errors in $d\omega/dx_{Na+Ca}$ up to 53% (Table 4). The data for sample S5 are excluded from fittings,
552 because this sample contains 0.32 apfu Cr^{3+}, which causes significant shifts by 5–10 cm^{-1} of all ^{V}OH
553 stretching modes. The derivative $d\omega/dx_{Na+Ca}$ is largest for overcharged YZZ species confirming that vacant
554 X sites preferably develop in the vicinity of overcharged triplets of octahedra. However, estimates of the X-
555 site occupancy in dravite can be more precisely determined from the dominant mode, because the relative
556 error in the $\omega(x_{Na+Ca})$ slope is smallest (see Table 4). The wavenumber of the ^{V}OH stretching mode arising
557 from the dominant YZZ triplet (3MgAlAl) as well as from 2MgAlAl-AlAlAl visually increases also with
558 the increase in the ^{X}Na/^{X}(Na+Ca) ratio (Fig. 9b), but the uncertainty in $d\omega/dx_{Na+Ca}$ obtained from linear fits
559 is too large to quantify the exact amount of ^{X}Na and ^{X}Ca in dravite.

560 The positions of the ^{V}OH-stretching peaks related to $3^{Y}Fe^{*Z}Al^{Z}Al$ and $2^{Y}Fe^{*Z}Al^{Z}Al$-$^{Y}Al^{Z}Al^{Z}Al$ in
561 schorl show no trends with the degree of X-site occupancy (Fig. 10a), indicating that these YZZ-YZZ-YZZ
562 species are exclusively associated with filled X sites in the proximity. In foitite, the positions of all three
563 main peaks, arising from $3^{Y}Fe^{*Z}Al^{Z}Al$, $2^{Y}Fe^{*Z}Al^{Z}Al$-$^{Y}Al^{Z}Al^{Z}Al$, and $^{Y}Fe^{*Z}Al^{Z}Al$-$2^{Y}Al^{Z}Al^{Z}Al$, exhibit
564 positive linear trends. As ^{Y}Al is the major substituent in both schorl and foitite, the positions of the ^{V}OH
565 stretching mode related to $^{Y}Fe^{*Z}Al^{Z}Al$-$2^{Y}Al^{Z}Al^{Z}Al$ species can be analyzed together. The distinctive
566 positive linear trend of ω versus ^{X}(Na+Ca) has only 7% relative error (Table 4). Thus, the content of filled
567 X sites per formula unit for both tourmaline species can be determined from the corresponding trend $\omega = ax$
568 + b given in Table 4. No dependencies of the ^{V}OH peaks on the normalized content of sodium could be
569 established, as most of the samples studied here are sodium dominated (Fig. 10b). The frequencies of the
570 ^{X}Ca-dominant Fe-bearing tourmaline adachiite (S43) strongly deviate from those of the corresponding
571 modes in schorl and foitite because of the substitution of Al for Si in the tetrahedral ring and thus cannot be
572 used to establish $\omega(x_{Na+Ca})$ or $\omega(x_{Na/(Na+Ca)})$ trends.

573 For elbaite and darrellhenryite, the dominant ^{V}OH mode related to the Li-rich species,
574 $2^{Y}Li^{Z}Al^{Z}Al$-$^{Y}Al^{Z}Al^{Z}Al$, shows a gradual increase in wavenumber with increasing the X-site occupancy,
575 whereas the wavenumber of this mode in fluor-liddicoatite clearly deviates from this trend (Fig. 11a). The

difference in the position of $2^{Y}Li^{Z}Al^{Z}Al$-$^{Y}Al^{Z}Al^{Z}Al$ in elbaite/darrellhenryite and fluor-liddicoatite maybe due to the fact that fluor-liddicoatite has for charge-balancing reasons another dominating mode at higher wavenumbers, which is assigned to $3^{Y}Li^{Z}Al^{Z}Al$. The content of occupied X sites per formula unit can be estimated for elbaite and darrellhenryite by the corresponding linear function given in Table 4, with a relative error in $d\omega/dx_{Na+Ca}$ of 27%. The dispersion of data points for the ^{V}OH peak related the $^{Y}Li^{Z}Al^{Z}Al$-$2^{Y}Al^{Z}Al^{Z}Al$ species is too large to establish any trend between the peak position and x_{Na+Ca}. Figure 11b shows a clear separation between the frequencies of the sodium-dominated elbaites and the calcium-dominated fluor-liddicoatite in dependence of the normalized sodium content $^{X}Na/^{X}(Na+Ca)$. The position of the ^{V}OH peak related to $2^{Y}Li^{Z}Al^{Z}Al$-$^{Y}Al^{Z}Al^{Z}Al$ remains constant, whereas a distinct shift to higher wavenumber with the increase in ^{X}Na is observed for fluor-liddicoatite. In contrast, the position of the ^{V}OH peak arising from $^{Y}Li^{Z}Al^{Z}Al$-$2^{Y}Al^{Z}Al^{Z}Al$ shifts to higher wavenumbers with the increase in ^{X}Ca for all Li-containing species. The trends in the wavenumber of this mode have been fitted separately for the alkali and calcic tourmaline species resulting in the same ω[Na/(Na+Ca)] slopes within the errors. Thus, the equation from combined fitting (Table 4) can be used to estimate the X-site occupying cation with the relative error of the slope being 22%.

For all tourmaline species, the frequencies of the ^{V}OH stretching modes related to the highest degree of ^{Y}Al substitution show the strongest influence depending on the ^{X}(Na+Ca) content. This implies that the corresponding YZZ configurations are predominantly associated with X-site vacancies, which is in line with the strongest overcharge of these triplets.

CONCLUSIONS

On the basis on the large suite of forty-six tourmaline samples from ten different subgroups studied here, we demonstrate that Raman scattering analysis of the framework and OH-stretching vibrations is a versatile tool for the identification of different tourmaline species. Peak positions and integrated intensities of the OH stretching vibrations can be used to determine the major X-site and Y-site cation occupancies. Moreover, the spectral shape, i.e. the occurrence of certain OH modes, is a good indicator for chemical disorder on the Y and Z as well as on the V and W site. As Raman spectroscopy is a non-

603 destructive, preparation-free, quick and easy-to-handle method, the following guidelines are intended to
604 help non-specialists to obtain crystallochemical data on tourmaline samples.

605 1.) Raman spectra with incident and scattered light polarized parallel to the *c* axis of the
606 tourmaline crystal should be taken in the spectral range 3000-4000 cm^{-1} and optionally between 100-1400
607 cm^{-1} with a satisfactory signal-to-noise ratio and a recommended spectral resolution of 2 cm^{-1} or better.

608 2.) Most of the tourmaline species can be identified by their spectral shape and peak positions,
609 without fitting the spectra, using e.g., Fig. 4 as reference. The overview of the Raman spectra of eleven
610 different tourmaline species in Fig. 4 can be used for comparison. Li-bearing tourmaline species are easily
611 identified by the two dominant ^{V}OH vibrations at 3494 cm^{-1} and 3593 cm^{-1} originating from $2^{Y}Li^{Z}Al^{Z}Al$-
612 $^{Y}Al^{Z}Al^{Z}Al$ and $^{Y}Li^{Z}Al^{Z}Al$-$2^{Y}Al^{Z}Al^{Z}Al$ species. While elbaite and darrellhenryite with comparable Fe*-
613 contents can hardly be distinguished without further chemical analysis, elbaite and fluor-liddicoatite can be
614 discriminated by the inspection of the peak positions. The strongest peak in fluor-liddicoatite is observed
615 above 3600 cm^{-1}, whereas in elbaite the dominant mode at higher wavenumbers is observed at 3593±4 cm^{-1}. $^{Y}(Fe^{2+}, Mn^{2+})$ impurities in elbaite or darrellhenryite can be immediately spotted by the presence of a
617 Raman peak near 3560 cm^{-1}.

618 The spectra of Mg-dominated species show one dominant ^{V}OH peak near 3575 cm^{-1} with two
619 shoulders at lower wavenumbers. If the samples are chemically close to the end-member compositions,
620 dravite and uvite can be distinguished by the position of the dominant ^{V}OH mode, which is observed at
621 3573±4 cm^{-1} in dravite and at 3579±2 cm^{-1} in uvite. However, if significant amounts of impurities, e.g., iron
622 are incorporated, the discrimination between these two species may be difficult without further analysis.

623 The ^{V}OH spectral shape of schorl is similar to that of Mg-dominated species, but the dominant
624 peak is observed at significantly lower wavenumber, 3566±1 cm^{-1}.

625 Foitite can be identified by the two strong ^{V}OH vibrations at 3551±1 and 3484±6 cm^{-1} in
626 combination with the doublet of ^{W}OH peaks at 3631±1 and 3644±1 cm^{-1}.

627 In Fe^{3+}-dominant species, the main ^{V}OH peak is significantly shifted to lower wavenumbers:
628 3531±1 cm^{-1} for fluor-buergerite and 3554±1 cm^{-1} for povondraite. For these species, it is helpful to
629 compare also the framework vibrations in Fig. 4.

630 Al-dominated olenite is characterized by the dominant ^{V}OH mode at 3455±1 cm^{-1}, which is the
631 lowest wavenumber of the dominant OH vibration for all tourmaline species.

632 3.) Quantitative analysis determination of the Y- and Z-site occupancies by Mg, (Fe^{2+}+Mn^{2+}), Al,
633 and Li can be achieved by fitting the Raman spectrum profiles in the OH-stretching wavenumber range
634 (3000-4000 cm^{-1}). For that purpose the spectra should be baseline corrected with a polynomial function and
635 fitted with pseudo-Voigt peak-shape functions. The maximum number of fitted peaks is given by the
636 intensity criterion $\Delta I < I/2$ with I being the peak intensity and ΔI the uncertainty. Temperature corrections
637 of the spectra are not necessary since at room temperature the influence of the Bose-Einstein distribution
638 factor is negligible above 500 cm^{-1}.

639 The ^{Y}Mg content in dravite can be calculated by
640 $^{Y}Mg\,(apfu) = (3I_{\omega(3573\,cm^{-1})} + 2I_{\omega(3534\,cm^{-1})} + I_{\omega(3494\,cm^{-1})}) / I_{^{V}OH_{total}}$, whereas the ^{Y}Al content can
641 be obtained from $^{Y}Al\,(apfu) = (I_{\omega(3534\,cm^{-1})} + 2I_{\omega(3494\,cm^{-1})}) / I_{^{V}OH_{total}}$ with I being the integrated
642 intensity of the peak at the given wavenumber and $I_{^{V}OH_{total}}$ the total integrated intensity of all ^{V}OH
643 stretching vibrations.

644 The Y-site iron content in schorl can be determined using the equation
645 $^{Y}Fe(apfu) = (3I_{\omega(3566\,cm^{-1})} + 2I_{\omega(3545\,cm^{-1})} + I_{\omega(3500\,cm^{-1})}) / I_{^{V}OH_{total}}$ and ^{Y}Al is given by
646 $^{Y}Al\,(apfu) = (I_{\omega(3545\,cm^{-1})} + 2I_{\omega(3500\,cm^{-1})}) / I_{^{V}OH_{total}}$. For foitite, $^{Y}Fe^{2+}$ can be calculated by
647 $^{Y}Fe(apfu) = (3I_{\omega(3570\,cm^{-1})} + 2I_{\omega(3551\,cm^{-1})} + I_{\omega(3484\,cm^{-1})}) / I_{^{V}OH_{total}}$ and ^{Y}Al by
648 $^{Y}Al\,(apfu) = (I_{\omega(3551\,cm^{-1})} + 2I_{\omega(3484\,cm^{-1})}) / I_{^{V}OH_{total}}$.

649 For elbaite, the ^{Y}Li content is calculated from the equation
650 $^{Y}Li(apfu) = (2I_{\omega(3593\,cm^{-1})} + I_{\omega(3494\,cm^{-1})}) / I_{^{V}OH_{total}}$. The ^{Y}Al content is given by
651 $^{Y}Al\,(apfu) = (I_{\omega(3593\,cm^{-1})} + 2I_{\omega(3494\,cm^{-1})} + I_{\omega(3562\,cm^{-1})} + 2I_{\omega(3465\,cm^{-1})}) / I_{^{V}OH_{total}}$ with the last two
652 terms in the sum being non-zero in the presence of Y-site iron and manganese. If so, the amounts of the
653 impurity iron and manganese can be inferred from
654 $^{Y}(Fe^{2+} + Mn^{2+})(apfu) = (2I_{\omega(3562\,cm^{-1})} + I_{\omega(3465\,cm^{-1})}) / I_{^{V}OH_{total}}$.

655 The uncertainties in the chemical-element amounts determined from the Raman data depend on
656 the quality of the measured spectra, including the spectral resolution and signal-to-noise ratio, as well as on

the goodness of fits, which may vary from specimen to specimen. For the data presented here the relative uncertainties vary between 2 % and 17 % depending on the amounts of minor and trace elements that were not taken into account in the calculation. The element amount determined by Raman spectroscopy is not biased by possible Y/Z-site disorder, but it refers to the Y-site occupancy in agreement with the calculation of the chemical formulae according to the currently accepted classification of tourmaline species (Henry et al. 2011).

These equations can be used for all other tourmaline species with slight modifications according to the corresponding peaks in the measured Raman spectra and using the peak assignment given in Fig. 5 and Table 3.

4) The content of ^{X}(Na+Ca) and thus the content of X-site vacancies can be determined from the position of the dominant ^{V}OH mode in dravite using the equation $\omega_{3573} = (30\pm10)x_{(Na+Ca)} + (3547\pm10)$. For schorl and foitite, x_{Na+Ca} can be determined from the positions of the ^{V}OH modes related to the ^{Y}Al-richest YZZ-YZZ-YZZ species near ω_{3500} and ω_{3484}, respectively, by the equation $\omega = (41\pm3)x_{(Na+Ca)} + (3467\pm2)$. The position of the dominant Li-bearing mode in elbaite and darrellhenryite near ω_{3593} can be used to quantify x_{Na+Ca}, using the equation $\omega_{3593} = (22\pm6)x_{(Na+Ca)} + (3576\pm4)$. An estimate of the X-site occupying cation is possible using the position of the second Li-bearing mode, ω_{3494} in elbaite and ω_{3511} in liddicaotite, by the equation $\omega = (39\pm15)x_{(Na/(Na+Ca))} + (3467\pm11)$.

5) The OH- tourmaline species can be qualitatively discriminated from fluor- and oxy-tourmalines via the number of ^{W}OH-stretching peaks. For alkali and calcic species, when there are no ^{W}OH-stretching peaks related to occupied X sites, then the sample is fluor-tourmaline if the Z- and Y-site occupancies, as determined from the ^{V}OH-stretching modes, do not allowed for $^{W}O^{2-}$ or it is oxy-tourmaline, if the Z- and Y-site occupancies suggest $^{W}O^{2-}$.

IMPLICATIONS

The two mineral supergroups: tourmalines and amphiboles are of great importance in Earth sciences as "geological DVDs" as well as in materials and environmental science. The analysis of the OH stretching vibrations of tourmaline by Raman spectroscopy showed that this is a well-suited analytical method for the identification of tourmaline species and determination of crystallochemial information. The

likewise successful application of this method in studying the OH stretching vibrations of amphiboles (Leißner et al. 2015) implies that the analysis of peak positions and intensities of certain vibrational groups has a great potential for the determination of the site occupancies in general in mineral supergroups, e.g., micas, epidotes, having OH groups bonded to cationic sites with variable chemistry. Compared to other analytical techniques, Raman spectroscopy combines the advantages of non-destructiveness, preparation-free, µm-scale analysis, quick and easy-to-handle experiments with simple data analysis. Thus, it can in particular be useful for samples for which cutting and polishing is undesirable or hardly possible.

Furthermore, this study demonstrates that the Raman-scattering analysis can reveal disordering of cations or anions over two sites in the crystal structure, which is commonly determined only by X-ray diffraction or quite often simply neglected. As it is shown here, the OH groups in tourmalines can be disordered over both V and W sites, although the chemical formulae calculated from EMPA data imply certain distributions. The consequent local over- or undercharge is compensated by preferred clustering of elements in the YYY and YZZ triplets in combination with the occupancy of the X site in the vicinity of these triplets. The ^{W}OH groups, which are positioned on the axis of symmetry the six-membered TO_4 rings show a preference for close-by vacant X sites, which are positioned on the same axis. It is quite likely that similar local clustering of certain elements to compensate element disorder over different sites in the crystal structure occurs also in other complex hydrous silicates such as micas.

Acknowledgements. Financial support by the Deutsche Forschungsgemeinschaft DFG (MI 1127/7-1 and SCHL 549/6-1) is gratefully acknowledged. The authors thank D. Nishio-Hamane, E. Lopatka, C. Schmidt and J. Clanin for providing tourmaline samples, P. Stutz for sample preparation for EMP and LA-ICP-MS measurements, S. Heidrich for conducting electron microprobe analysis, and F. Keilflug for parts of the Raman spectroscopic measurements. We are also grateful for the constructive reviews by D. Henry and F. Bosi, which helped to improve the quality of the manuscript. In particular, we would like to acknowledge the efforts of F. Bosi in extensive discussions on atomic bonding and disorder in tourmalines. R. Stalder is thanked for the editorial handling of the manuscript.

References

Alvarez M.A., and Coy-Yll, R. (1977) Raman spectra of tourmaline. Spectrochimica Acta, 34A, 899-908.

Berryman E.J., Wunder B., Ertl, A., Koch-Müller, M., Rhede, D., Scheidl, K., Giester, G., and Heinrich, W. (2015) Influence of the X-site composition on tourmaline's crystal structure: investigation of synthetic K-dravite, dravite, oxy-uvite, and magnesio-foitite using SREF and Raman spectroscopy. Physics and Chemistry of Minerals, doi: 10.1007/s00269-015-0776-3.

Bosi, F., and Lucchesi, S. (2007) Crystal chemical relationships in the tourmaline group: structural constraints on chemical variability. American Mineralogist, 92, 1054-1063.

Bosi, F. (2013) Bond-valence constraints around the O1 site of tourmaline. Mineralogical Magazine, 77, 343-351.

Bosi, F., Skogby, H., Agrosì, G., and Scandale, E. (2012) Tsilaisite, $NaMn_3Al_6(Si_6O_{18})(BO_3)_3(OH)_3OH$, a new mineral species of the tourmaline supergroup from Grotta d'Oggi, San Piero in Campo, island of Elba, Italy. American Mineralogist, 97, 989-994.

Bosi, F., Skogby, H., Lazor, P., and Reznitskii, L. (2015a) Atomic arrangements around the O3 site in Al- and Cr-rich oxy-tourmalines: a combined EMP, SREF, FTIR and Raman study. Physics and Chemistry of Minerals, 42, 441-453.

Bosi, F., Andreozzi, G.B., Hålenius, U., and Skogby, H. (2015b) Experimental evidence for partial Fe^{2+} disorder at the Y and Z sites of tourmaline: a combined EMP, SREF, MS, IR and OAS study of schorl. Mineralogical Magazine, 79, 515-528.

Brese, N.E., and O'Keeffe, M. (1991) Bond-valence parameters for solids. Acta Crystallographica, B47, 192-197.

Castañeda, C., Oliveira, E.F., Gomes, N., and Soares, A.C.P. (2000) Infrared study on OH sites in tourmaline from the elbaite-schorl series. American Mineralogist, 85, 1503-1507.

Chang, I.F., and Mitra, S.S. (1971) Long wavelength optical phonons in mixed crystals. Advances in Physics, 20, 359-404.

Colopietro, M.R., and Friberg, L.M. (1987) Tourmaline-biotite as a potential geothermometer for metapelites, Black Hills, South Dakota. Geological Society of America, Abstract Programs, 19, 624.

Donnay, G., Ingamells, C.O., and Mason, B. (1996) Buergerite, a new species of tourmaline. American Mineralogist, 51, 198-199.

Dutrow, B.L., and Henry, D.J. (2011) Tourmaline: A geological DVD. Elements, 7, 301-306.

Ertl, A., Hughes, J.M., Prowatke, S., Ludwig, T., Prasad, P.S.R., Brandstaetter, F., Koerner, W., Schuster, R., Pertlik, F., and Marschall, H. (2006) Tetrahedrally coordinated boron in tourmalines from the liddicoatite-elbaite series from Madagascar: structure, chemistry and infrared spectroscopic studies. American Mineralogist, 91, 1847-1856.

Ertl, A., Tillmanns, E., Ntaflos, T., Francis, C., Giester, G., Körner, W., Hughes, J.M., Lengauer, C., and Prem, M. (2008) Tetrahedrally coordinated boron in Al-rich tourmaline and its relationship to the pressure-temperature conditions of formation. European Journal of Mineralogy, 20, 881-888.

Ertl, A., Marschall, H.R., Giester, G., Henry, D.J., Schertl, H.-P., Ludvizotto, G.L., Nasdala, L., and Tillmanns, E. (2010) Metamorphic ultrahigh-pressure tourmaline: structure, chemistry, and correlation to *P-T* conditions. American Mineralogist, 95, 1-10.

Fantini, C., Tavares, M.C., Krambrock, K., Moreira, R.L., and Righi, A. (2014) Raman and infrared study of hydroxyl sites in natural uvite, fluor-uvite, magnesio-foitite, dravite and elbaite tourmalines. Physics and Chemistry of Minerals, 41, 247-254.

Gasharova, B., Mihailova, B., and Konstantinov, L (1997) Raman spectra of various types of tourmaline. European Journal of Mineralogy, 9, 935-940.

Gatta, G.D., Bosi, F., McIntyre, G.J. and Skogby, H. (2014) First accurate location of two proton sites in tourmaline: a single-crystal neutron diffraction study of oxy-dravite. Mineralogical Magazine, 78, 681–692.

Gonzalez-Carreño, T., Fernandez, M., and Sanz, J. (1988) Infrared and electron microprobe analysis in tourmalines. Physics and Chemistry of Minerals, 15, 452-460.

762 Grice, J.D., and Ercit, T.S. (1993) Ordering of Fe and Mg in the tourmaline crystal structure: The correct
763 formula. Neues Jahrbuch Mineralogische Abhandlungen, 165, 245-266.
764 Hawthorne, F.C. (1996) Structural mechanisms for light-element variations in tourmaline. Canadian
765 Mineralogist, 34, 123-132.
766 Hawthorne, F.C., and Dirlam, D.M. (2011) Tourmaline the indicator mineral: From atomic arrangement to
767 Viking navigation. Elements, 7, 307-312.
768 Hawthorne, F.C., MacDonald, D.J., and Burns, P.C. (1993) Reassignment of cation site occupancies in
769 tourmaline: Al-Mg disorder in the crystal structure of dravite. American Mineralogist, 78, 265-
770 270.
771 Hawthorne, F.C., Della Ventura, G., and Robert, J.-L. (1996) Short-range order of (Na,K) and Al in
772 tremolite: An infrared study. American Mineralogist, 81, 782-784.
773 Henry, D.J., and Dutrow, B.L. (1996) Metamorphic tourmaline and its petrologic applications. In E.S.
774 Grew and L.M. Anovitz, Eds., Boron: Mineralogy, Petrology and Geochemistry, 33, p. 503-557.
775 Reviews in Mineralogy, Mineralogical Society of America, Chantilly, Virginia.
776 Henry, D.J., and Dutrow, B.L. (2001) Compositional zoning and element partitioning in nickeloan
777 tourmaline from a metamorphosed karstbauxite from Samos, Greece. American Mineralogist, 80,
778 1130-1142.
779 Henry, D.J., and Dutrow, B.L. (2011) The incorporation of fluorine in tourmaline: internal crystallographic
780 controls or external environmental influences? Canadian Mineralogist, 49, 41-56.
781 Henry, D.J., Kirkland, B.L., and Kirlkand, D.W. (1999) Sector-zoned tourmaline from the cap rock of a salt
782 dome. European Journal of Mineralogy, 11, 263-280.
783 Henry, D.J., Novák, M., Hawthorne, F.C., Ertl, A., Dutrow, B.L., Uher, P., and Pezzotta, F. (2011)
784 Nomenclature of the tourmaline-supergroup minerals. American Mineralogist, 96, 895-913.
785 Hoang, L.H., Hien, N.T.M., Chen, X.B., Minh, N.V., and Yang, I.-S. (2011) Raman spectroscopic study of
786 various types of tourmalines. Journal of Raman Spectroscopy, 42, 1442-1446.
787 Hofmeister, A.M., and Chopelas A. (1991) Vibrational spectroscopy of end-member silicate garnets.
788 Physics and Chemistry of Minerals, 17, 503-526.

Horn, I., von Blanckenburg, F., Schoenberg, R., Steinhöfel, G., and Markl, G. (2006) In situ iron isotope ratio determination using UV-femtosecond laser ablation with application to hydrothermal ore formation processes. Geochimica et Cosmochimica Acta, 70, 3677-3688.

Kawakami, T., and Ikeda, T. (2003) Boron in metapelites controlled by the breakdown of tourmaline and retrograde formation of borosilicates in the Yanai area, Ryoke metamorphic belt, SW Japan. Contributions to Mineralogy and Petrology, 145, 131-150.

Keller, P., Roda Robles, E., Pesquera Pérez, A., and Fontan, F. (1999) Chemistry, paragenesis and significance of tourmaline in pegmatites of the Southern tin belt, central Namibia. Chemical Geology, 158, 203-225.

Kroumova, E., Aroyoy, M.I., Perez Mato, J.M., Kirov, A., Capillas, C., Ivantchev, S., and Wondratschek, H. (2003) Bilbao Crystallographic Server: useful databases and tools for phase transitions studies. Phase Transitions, 76, 155-170.

Kuzmany, H. (2009) Solid-state spectroscopy – An introduction, p. 554. Springer, Berlin Heidelberg.

Leißner, L., Schlüter, J., Horn, I, and Mihailova, B. (2015) Exploring the potential of Raman spectroscopy for crystallochemical analyses of complex hydrous silicates: I. Amphiboles. American Mineralogist, in press.

Liu Y.S., Hu Z.C., Gao S., Gu□nther D., Xu J., Gao C.G., and Chen H.H. (2008) In situ analysis of major and trace elements of anhydrous minerals by LA-ICP-MS without applying an internal standard. Chemical Geology, 257, 34-43.

London, D. (2011) Experimental synthesis and stability of tourmaline: ahistorical perspective. Canadian Mineralogist, 49, 117-136.

Malcherek, T., and Schlüter, J. (2007) $Cu_3MgCl_2(OH)_6$ and the bond-valence parameters of the OH-Cl bond. Acta Crystallographica, B63, 157-160.

Marschall, H.R., Korsakov, A.V., Luvizotto, G.L., Nasdala, L., and Ludwig, T. (2009) On the occurrence and boron isotopic composition of tourmaline in (ultra)high-pressure metamorphic rocks. Journal of the Geological Society, 166, 811-823.

Martìnez-Alonso, S., Rustad, J.R., Goetz, A.F.H. (2002) Ab initio quantum mechanical modeling of infrared vibrational frequencies of the OH group in dioctahedral phyllosilicates. Part II: main physical factors governing the OH vibration. American Mineralogist, 87, 1224-1234.

McKeown, D.A. (2008) Raman spectroscopy, vibrational analysis, and heating of buergerite tourmaline. Physics and Chemistry of Minerals, 35, 259-270.

Mernagh, T.P. (1991) Use of the laser Raman microprobe for discrimination amongst feldspar minerals. Journal of Raman Spectroscopy, 22, 453-457.

Mihailova, B., Gasharova, B., and Konstantinov, L. (1996) Influence on non-tetrahedral cations in Si–O vibrations in complex silicates. Journal of Raman Spectroscopy, 27, 829-833.

Momma, K., and Izumi, F. (2011) VESTA 3 for three-dimensional visualization of crystal, volumetric and morphology data. Journal of Applied Crystallography, 44, 1272-1276.

Nishio-Hamane, D., Minakawa, T., Yamaura, J-i, Oyama, T., Ohnishi, M., and Shimobayashi, N. (2014) Adachiite, a Si-poor member of the tourmaline supergroup from the Kiura mine, Oita prefecture, Japan. Journal of Mineralogical and Petrological Sciences, 109, 74-78.

Oeser, M., Dohmen, R., Horn, I., Schuth, S., and Weyer, S. (2015) Processes and time scales of magmatic evolution as revealed by Fe-Mg chemical and isotopic zoning in natural olivines. Geochimica et Cosmochimica Acta, 154, 130-150.

Oliveira, E.F., Castañeda C, Eeckhout, S.G., Gilmar, M.M., Kwitko, R.R., de Grave, E., and Botelho, N.F. (2002) Infrared and Mössbauer study of Brazilian tourmalines from different geological environments. American Mineralogist, 87, 1154-1163.

Petricek, V., Dusek, M., and Palatinus, L. (2014) Crystallographic computing system JANA2006: General features. Zeitschrift für Kristallographie, 229, 345-352.

Schreurs, A.M.M., Xian, X., and Kroon-Batenburg, L.M.J. (2010) EVAL15: a diffraction data integration method based on ab initio predicted profiles. Journal of Applied Crystallography, 43, 70-82.

Selway, J.B. Novák, M., Černý, P., and Hawthorne, F.C. (1999) Compositional evolution of tourmaline in lepidolite-subtype pegmatites. European Journal of Mineralogy, 11, 596-584.

Selway, J.B., Černý, P., and Hawthorne, F.C. (2000) The Tanco pegmatite at Bernic lake, Manitoba. XIV. International tourmaline conference. Canadian Mineralogist, 38, 877-891.

Shannon, R.D. (1976) Revised effective ionic radii and systematic studies of interatomic distances in halides and chalcogenides. Acta Crystallographica, A32, 751-767.

Slack, J.F. (1996) Tourmaline associations with hydrothermal ore deposits. In E.S. Grew and L.M. Anovitz, Eds., Boron: Mineralogy, Petrology and Geochemistry, 33, p. 559-644. Reviews in Mineralogy, Mineralogical Society of America, Chantilly, Virginia.

Skogby, H., Bosi, F., and Lazor, P. (2012) Short-range order in tourmaline: a vibrational spectroscopic approach to elbaite. Physics and Chemistry of Minerals, 39, 811-816.

Trumbull, R.B., Slack, J.F., Krienitz, M.-S., Belkin, H.E., and Wiedenbeck, M. (2011) Fluid sources and metallogenesis in the Blackbird Co-Cu-Au-Bi-Y-REE district, Idaho, USA: insights from major-element and boron isotopic compositions of tourmaline. Canadian Mineralogist, 49, 225-244.

van Hinsberg, V.J., and Marschall, H.R. (2007) Boron isotope and light element sector zoning in tourmaline: implications for the formation of B-isotopic signatures. Chemical Geology, 238, 141-148.

van Hinsberg, V.J., and Schumacher, J.C. (2007) Intersector element partitioning in tourmaline: a potentially powerful single crystal thermometer. Contributions to Mineralogy and Petrology, 153, 289-301.

van Hinsberg, V.J., Henry, D.J., and Marschall, H.R. (2011) Tourmaline: An ideal indicator of its host environment. Canadian Mineralogist, 49, 1-16.

Wang, A., Jolliff B.L., Haskin, L.A., Kuebler, K.E., and Viskupic, K.M. (2001) Characterization and comparison of structural and compositional features of planetary quadrilateral pyroxenes by Raman spectroscopy. American Mineralogist, 86, 90-806.

Williamson, B.J., Spratt, J., Adams, J.T., Tindle, A.G., and Stanley, C.J. (2000) Geochemical constraints from zoned hydrothermal tourmaline on fluid evolution and Sn mineralization: an example from fault breccias at Roche, SW England. Journal of Petrology, 41, 1439-1453.

867 Yavuz, F., Karakaya, N., Yıldırım, D.K., Karakaya, M.Ç., and Kumral, M. (2014) A Windows program for
868 calculation and classification of tourmaline-supergroup (IMA-2011). Computers and Geosciences,
869 63, 70-87.
870 Zhao, C., Liao, L., Xia, Z., and Sun, X. (2012) Temperature-dependent Raman and infrared spectroscopy
871 study on iron-magnesium tourmaline with different Fe content. Vibrational Spectroscopy, 62, 28-
872 34.
873

874 **Figure captions**

875

876 **Figure 1.** Crystal structure of tourmaline with rhombohedral symmetry (*R*3*m*); X-site cations are given in
877 yellow, Y-site octahedra in brown, Z-site octahedra in light blue, TO_4 tetrahedra in dark blue, BO_3 groups
878 in green, oxygen atoms are shown in red, hydrogen in rose. The V and W sites are marked by the black
879 ellipses and are occupied here by OH groups. The structural data were taken from Ertl et al. (2006) and the
880 software package VESTA (Momma and Izumi 2011) was used for figure preparation.

881

882 **Figure 2.** Comparison of B_2O_3 and Li_2O contents measured by LA ICP-MS and calculated from the EMPA
883 data (see text for details). The horizontal error bars represent the statistical deviation on the EMPA values,
884 whereas the vertical error bars correspond to the experimental accuracy of the ICP-MS data (5% relative
885 error). The gray lines mark the one-to-one correlations.

886

887 **Figure 3**. Polarized Raman spectra of dravite (S2) measured in five scattering geometries given in Porto's
888 notation $k_i(E_iE_s)k_s$ with k_i = propagation of incident light, E_i = polarization of incident light, E_S =
889 polarization of scattered light, k_s = propagation of scattered light. Spectra are vertically offset for clarity.

890

891 **Figure 4**. Polarized $\bar{y}(zz)y$ Raman spectra of representative tourmaline species. For better comparison the
892 spectra are normalized to the intensity of the dominant Al–O stretching vibration at 365-375 cm^{-1} except
893 S33, which is normalized to the Fe-O stretching vibration at 222 cm^{-1}, and are vertically offset for clarity.
894 The prefix "F-" in the plot stands for "fluor-". Note that sample S18 is a (Fe+Mg)-containing fluor-elbaite.

895

896 **Figure 5.** Peak assignment of the Raman active O–H stretching modes of a) dravite (S3), b) fluor-uvite
897 (39), c) schorl (S8), d) foitite (S44), e) fluor-elbaite (S18), and f) fluor-liddicoatite (S40). The prefix "F-" in
898 the plots stands for "fluor-". The superscripted letters designate the corresponding site in the general
899 tourmaline formula. Fe* is used as abbreviation for (Fe^{2+}+Mn^{2+}).

900

Figure 6. Behavior of (a) the mean ionic radius $<r_{YZZ}>$ of the triplet of YZZ octahedra and (b) the mean ionic radius $<r_{YYY}>$ of the YYY octahedral triplet with the wavenumber of the OH stretching mode related to a given chemical species, averaged over the tourmaline samples; the error bars represent statistical deviations. $<r_{YZZ}>$ and $<r_{YYY}>$ are calculated using the ionic radii for the Y- and Z-site cations in tourmalines by Bosi and Lucchesi (2007). Note that the given Y and Z site allocations for uvite (purple circles) is the one used for the calculation of the mean ionic radius.

Figure 7. Major Y-site cation contents in atoms per formula unit of a) magnesium, b) divalent iron plus manganese, c) lithium, and d) aluminum calculated from the integrated intensities of the assigned vibrational modes in the Raman spectra versus the corresponding contents measured by EMPA ($^{Y}Li_{EMPA\ calc.}$ is the Li content calculated EPMA data). Tourmaline species are shown in different symbol colors according to the legend in a). One-to-one correlations are indicated by the black dashed lines.

Figure 8. Ratio of the integrated intensities of the ^{V}OH peaks arising from $2^{Y}Fe^{*Z}Al^{Z}Al\text{-}^{Y}Al^{Z}Al^{Z}Al$ and $2^{Y}Li^{Z}Al^{Z}Al\text{-}^{Y}Al^{Z}Al^{Z}Al$ species in elbaite as a function of $^{Y}(Fe^{2+}+Mn^{2+})$ per formula unit from EMPA. Data points with red contours are excluded from fitting (see the text). Gray lines represent linear fits.

Figure 9. Positions of the ^{V}OH stretching modes related to $3^{Y}Mg^{Z}Al^{Z}Al$ (circles), $2^{Y}Mg^{Z}Al^{Z}Al\text{-}^{Y}Al^{Z}Al^{Z}Al$ (squares), and $^{Y}Mg^{Z}Al^{Z}Al\text{-}2^{Y}Al^{Z}Al^{Z}Al$ (diamonds) in dravite versus the content of a) ^{X}(Na+Ca) per formula unit and b) $^{X}Na/^{X}$(Na+Ca) obtained from EMPA. The data points with the orange contours stem from sample S5, a dravite with ^{Y}Cr instead of ^{Y}Al, and are excluded from fitting. Linear fits are given by gray lines.

Figure 10. Positions of the ^{V}OH stretching modes related to $3^{Y}Fe^{*Z}Al^{Z}Al$ (circles), $2^{Y}Fe^{*Z}Al^{Z}Al\text{-}^{Y}Al^{Z}Al^{Z}Al$ (squares), and $^{Y}Fe^{*Z}Al^{Z}Al\text{-}2^{Y}Al^{Z}Al^{Z}Al$ (diamonds) of schorl (green) and foitite (blue) versus the content of a) ^{X}(Na+Ca) per formula unit and b) $^{X}Na/^{X}$(Na+Ca) obtained from EMPA. Fe^{2+} and Mn^{2+} are

considered together as Fe* in the species names. Data points with red contours are excluded from fitting (see text). Linear fits are given by gray lines.

Figure 11. Positions of the ^{V}OH stretching modes related to $3^{Y}Li^{Z}Al^{Z}Al$ (circles), $2^{Y}Li^{Z}Al^{Z}Al$-$^{Y}Al^{Z}Al^{Z}Al$ (squares), and $^{Y}Li^{Z}Al^{Z}Al$-$2^{Y}Al^{Z}Al^{Z}Al$ (diamonds) of elbaite (orange), fluor-liddicoatite (light blue), and darrellhenryite (light pink) versus the content of a) ^{X}(Na+Ca) per formula unit and b) ^{X}Na/^{X}(Na+Ca) obtained from EPMA. Data points with red contours are excluded from fitting (see text). Linear fits are given by gray lines.

Table 1. Chemical compositions of the studied tourmaline samples determined by electron microprobe analysis

Samples	Name (IMA2011)	General tourmaline formula $XY_3Z_6(T_6O_{18})(BO_3)_3V_3W$					
		X	Y_3	Z_6	T_6	V_3	W
alkali-subgroup 1							
S1	Dravite	$Na_{0.79\pm0.01}\square_{0.12\pm0.01}Ca_{0.08\pm0.01}$	$Mg_{2.67\pm0.02}Al_{0.24\pm0.03}Fe_{0.04\pm0.01}Ti_{0.03\pm0.01}$	Al_6	Si_6	$(OH)_3$	$(OH)_{0.76\pm0.02}F_{0.11\pm0.02}O_{0.12\pm0.01}$
S2	Dravite	$Na_{0.76\pm0.02}Ca_{0.13\pm0.01}\square_{0.12\pm0.01}$	$Mg_{2.71\pm0.02}Al_{0.18\pm0.02}Fe_{0.05\pm0.01}Ti_{0.04\pm0.01}$	Al_6	$Si_{6.02\pm0.01}$	$(OH)_3$	$(OH)_{0.76\pm0.03}F_{0.13\pm0.02}O_{0.12\pm0.01}$
S3	Dravite	$Na_{0.61\pm0.01}\square_{0.22\pm0.02}Ca_{0.16\pm0.01}$	$Mg_{2.45\pm0.02}Al_{0.44\pm0.02}Ti_{0.05\pm0.01}Cr_{0.04\pm0.01}$	Al_6	$Si_{5.98\pm0.02}Al_{0.03\pm0.01}$	$(OH)_3$	$(OH)_{0.65\pm0.02}F_{0.13\pm0.02}O_{0.22\pm0.01}$
S4	Dravite	$Na_{0.65\pm0.01}\square_{0.22\pm0.01}Ca_{0.12\pm0.01}$	$Mg_{2.26\pm0.02}Al_{0.67\pm0.02}Ti_{0.05\pm0.01}$	Al_6	$Si_{6\pm0.01}$	$(OH)_3$	$(OH)_{0.66\pm0.03}F_{0.11\pm0.02}O_{0.23\pm0.02}$
S5	Dravite	$Na_{0.46\pm0.01}Ca_{0.39\pm0.01}\square_{0.13\pm0.01}$	$Mg_{2.65\pm0.01}Cr_{0.27\pm0.01}Ti_{0.03\pm0.01}$	$Al_{5.95\pm0.01}Cr_{0.05\pm0.01}$	$Si_{5.93\pm0.02}Al_{0.07\pm0.02}$	$(OH)_3$	$(OH)_{0.78\pm0.02}F_{0.09\pm0.01}O_{0.13\pm0.01}$
S6	Schorl	$Na_{0.64\pm0.04}\square_{0.30\pm0.05}Ca_{0.05\pm0.01}$	$Fe_{1.88\pm0.08}Al_{0.46\pm0.1}Mg_{0.36\pm0.06}Ti_{0.03\pm0.01}$	Al_6	$Si_{5.93\pm0.03}Al_{0.07\pm0.03}$	$(OH)_3$	$(OH)_{0.62\pm0.03}F_{0.07\pm0.03}O_{0.30\pm0.05}$
S7	F-Schorl	$Na_{0.68\pm0.01}\square_{0.23\pm0.02}Ca_{0.08\pm0.01}$	$Fe_{2.38\pm0.06}Al_{0.44\pm0.05}Mg_{0.09\pm0.01}Ti_{0.08\pm0.01}Mn_{0.02\pm0.01}$	Al_6	Si_6	$(OH)_3$	$F_{0.55\pm0.03}O_{0.23\pm0.02}(OH)_{0.22\pm0.02}$
S8	F-Schorl	$Na_{0.76\pm0.1}\square_{0.22\pm0.1}$	$Fe_{2.72\pm0.1}Al_{0.24\pm0.1}Mg_{0.02\pm0.01}$	Al_6	$Si_{5.93\pm0.04}Al_{0.07\pm0.03}$	$(OH)_3$	$F_{0.53\pm0.20}(OH)_{0.25\pm0.1}O_{0.22\pm0.1}$
S9	F-Schorl	$Na_{0.72\pm0.02}\square_{0.18\pm0.02}Ca_{0.10\pm0.01}$	$Fe_{2.58\pm0.06}Al_{0.61\pm0.08}Ti_{0.08\pm0.01}Mg_{0.07\pm0.01}Mn_{0.03\pm0.01}$	Al_6	Si_6	$(OH)_{2.52\pm0.08}O_{0.49\pm0.08}$	$F_{0.66\pm0.03}O_{0.35\pm0.03}$
S10	F-Schorl	$Na_{0.93\pm0.01}\square_{0.06\pm0.01}$	$Fe_{1.75\pm0.04}Al_{0.94\pm0.05}Li_{0.26\pm0.06}Ti_{0.03\pm0.01}$	Al_6	Si_6	$(OH)_{2.89\pm0.08}O_{0.11\pm0.08}$	$F_{0.79\pm0.03}O_{0.21\pm0.03}$
alkali-subgroup 2							
S11	Elbaite	$Na_{0.57\pm0.02}\square_{0.41\pm0.02}$	$Al_{1.61\pm0.05}Li_{0.91\pm0.03}Mn_{0.46\pm0.04}Ti_{0.02\pm0.01}$	Al_6	Si_6	$(OH)_3$	$(OH)_{0.43\pm0.08}F_{0.26\pm0.05}O_{0.31\pm0.09}$
S12	Elbaite	$Na_{0.56\pm0.03}\square_{0.43\pm0.03}Ca_{0.02\pm0.01}$	$Al_{2.12\pm0.07}Li_{0.84\pm0.07}Mn_{0.02\pm0.01}$	Al_6	Si_6	$(OH)_3$	$(OH)_{0.50\pm0.09}F_{0.24\pm0.05}O_{0.27\pm0.07}$
S13	F-Elbaite	$Na_{0.54\pm0.01}\square_{0.38\pm0.01}Ca_{0.08\pm0.01}$	$Al_{1.57\pm0.05}Li_{1.33\pm0.04}Fe_{0.06\pm0.01}Mn_{0.06\pm0.01}$	Al_6	Si_6	$(OH)_{2.74\pm0.04}O_{0.26\pm0.04}$	$F_{0.56\pm0.03}O_{0.44\pm0.03}$
S14	F-Elbaite	$Na_{0.52\pm0.01}\square_{0.43\pm0.01}Ca_{0.05\pm0.01}$	$Al_{2.06\pm0.03}Li_{0.91\pm0.06}Mn_{0.03\pm0.01}$	Al_6	Si_6	$(OH)_3$	$F_{0.35\pm0.02}O_{0.35\pm0.03}(OH)_{0.31\pm0.04}$
S15	F-Elbaite	$Na_{0.83\pm0.01}\square_{0.09\pm0.01}Ca_{0.08\pm0.01}$	$Al_{1.47\pm0.03}Mn_{0.71\pm0.02}Li_{0.44\pm0.04}Fe_{0.33\pm0.02}Mg_{0.03\pm0.01}Ti_{0.03\pm0.01}$	Al_6	Si_6	$(OH)_{2.74\pm0.06}O_{0.26\pm0.06}$	$F_{0.73\pm0.04}O_{0.27\pm0.04}$
S16	F-Elbaite	$Na_{0.63\pm0.01}\square_{0.29\pm0.01}Ca_{0.08\pm0.01}$	$Al_{1.85\pm0.05}Li_{0.78\pm0.04}Mn_{0.36\pm0.03}$	Al_6	Si_6	$(OH)_3$	$F_{0.49\pm0.03}(OH)_{0.44\pm0.05}O_{0.07\pm0.04}$
S17	F-Elbaite	$Na_{0.66\pm0.04}\square_{0.31\pm0.05}Ca_{0.04\pm0.01}$	$Al_{1.67\pm0.09}Li_{1.06\pm0.06}Mn_{0.26\pm0.11}$	Al_6	Si_6	$(OH)_3$	$F_{0.47\pm0.06}O_{0.37\pm0.09}(OH)_{0.16\pm0.07}$
S18	F-Elbaite	$Na_{0.73\pm0.02}\square_{0.22\pm0.01}Ca_{0.05\pm0.01}$	$Al_{1.45\pm0.06}Li_{1.01\pm0.05}Fe_{0.36\pm0.03}Mn_{0.18\pm0.03}$	Al_6	Si_6	$(OH)_3$	$F_{0.67\pm0.02}O_{0.23\pm0.05}(OH)_{0.10\pm0.06}$
S19	F-Elbaite	$Na_{0.80\pm0.01}\square_{0.16\pm0.01}Ca_{0.03\pm0.01}$	$Al_{1.25\pm0.04}Li_{1.01\pm0.04}Fe_{0.50\pm0.01}Mn_{0.22\pm0.01}$	Al_6	Si_6	$(OH)_3$	$F_{0.72\pm0.03}O_{0.17\pm0.04}(OH)_{0.11\pm0.04}$
S20	F-Elbaite	$Na_{0.69\pm0.02}Ca_{0.17\pm0.05}\square_{0.14\pm0.03}$	$Al_{1.35\pm0.1}Li_{1.09\pm0.09}Mn_{0.37\pm0.02}Fe_{0.16\pm0.01}Mg_{0.02\pm0.01}$	Al_6	Si_6	$(OH)_{2.92\pm0.07}O_{0.09\pm0.07}$	$F_{0.86\pm0.05}O_{0.14\pm0.06}$
S21	F-Elbaite	$Na_{0.52\pm0.02}\square_{0.28\pm0.02}Ca_{0.20\pm0.03}$	$Al_{1.67\pm0.05}Li_{1.20\pm0.05}Mn_{0.13\pm0.01}$	Al_6	Si_6	$(OH)_{2.89\pm0.07}O_{0.11\pm0.07}$	$F_{0.63\pm0.03}O_{0.37\pm0.03}$
S22	F-Elbaite	$Na_{0.48\pm0.02}Ca_{0.26\pm0.05}\square_{0.26\pm0.02}$	$Al_{1.91\pm0.07}Li_{0.97\pm0.08}Mn_{0.11\pm0.01}$	Al_6	Si_6	$(OH)_3$	$F_{0.61\pm0.04}O_{0.24\pm0.10}(OH)_{0.16\pm0.08}$
S23	F-Elbaite	$Na_{0.54\pm0.01}\square_{0.30\pm0.05}Ca_{0.16\pm0.04}$	$Al_{1.80\pm0.13}Li_{1.01\pm0.07}Mn_{0.17\pm0.09}$	Al_6	Si_6	$(OH)_{3\pm0.04}$	$F_{0.60\pm0.05}O_{0.30\pm0.06}(OH)_{0.10\pm0.06}$
S24	F-Elbaite	$Na_{0.57\pm0.02}\square_{0.38\pm0.02}Ca_{0.05\pm0.01}$	$Al_{1.50\pm0.03}Li_{1.43\pm0.03}Mn_{0.05\pm0.01}$	Al_6	Si_6	$(OH)_{2.60\pm0.06}O_{0.40\pm0.05}$	$F_{0.59\pm0.03}O_{0.41\pm0.03}$
S25	F-Elbaite	$Na_{0.49\pm0.01}Ca_{0.26\pm0.02}\square_{0.25\pm0.01}$	$Al_{1.62\pm0.06}Li_{1.36\pm0.06}Mn_{0.02\pm0.01}$	Al_6	Si_6	$(OH)_{2.76\pm0.07}O_{0.26\pm0.07}$	$F_{0.63\pm0.03}O_{0.37\pm0.03}$
S26	F-Elbaite	$Na_{0.67\pm0.03}\square_{0.19\pm0.02}Ca_{0.13\pm0.04}$	$Al_{0.85\pm0.04}Li_{1.40\pm0.04}Fe_{0.37\pm0.04}Mg_{0.32\pm0.05}Mn_{0.05\pm0.02}Ti_{0.02\pm0.01}$	Al_6	Si_6	$(OH)_{2.89\pm0.05}O_{0.11\pm0.05}$	$F_{0.52\pm0.06}O_{0.48\pm0.06}$
S27	F-Elbaite	$Na_{0.86\pm0.01}\square_{0.09\pm0.01}Ca_{0.06\pm0.01}$	$Al_{1.09\pm0.04}Li_{0.91\pm0.04}Fe_{0.74\pm0.02}Mn_{0.22\pm0.02}Mg_{0.03\pm0.01}Ti_{0.02\pm0.01}$	Al_6	Si_6	$(OH)_{2.65\pm0.05}O_{0.35\pm0.05}$	$F_{0.79\pm0.03}O_{0.21\pm0.05}$
S28	F-Elbaite	$Na_{0.77\pm0.01}\square_{0.19\pm0.01}Ca_{0.04\pm0.01}$	$Al_{1.38\pm0.03}Li_{0.82\pm0.04}Fe_{0.55\pm0.01}Mn_{0.15\pm0.01}Mg_{0.10\pm0.01}$	Al_6	Si_6	$(OH)_{2.77\pm0.3}O_{0.23\pm0.3}$	$F_{0.65\pm0.03}(OH)_{0.21\pm0.16}O_{0.15\pm0.15}$
S29	F-Elbaite	$Na_{0.77\pm0.01}\square_{0.20\pm0.01}Ca_{0.03\pm0.01}$	$Al_{1.27\pm0.02}Li_{0.92\pm0.03}Fe_{0.58\pm0.01}Mn_{0.22\pm0.02}$	Al_6	Si_6	$(OH)_3$	$F_{0.58\pm0.03}(OH)_{0.29\pm0.05}O_{0.13\pm0.03}$
S30	F-Elbaite	$Na_{0.65\pm0.01}Ca_{0.25\pm0.01}\square_{0.09\pm0.01}$	$Al_{1.31\pm0.03}Li_{1.05\pm0.03}Mn_{0.61\pm0.02}Ti_{0.03\pm0.01}$	Al_6	Si_6	$(OH)_3$	$F_{0.58\pm0.04}O_{0.14\pm0.04}(OH)_{0.07\pm0.05}$
S31	F-Elbaite	$Na_{0.86\pm0.01}\square_{0.09\pm0.02}Ca_{0.05\pm0.01}$	$Al_{1.27\pm0.03}Li_{0.69\pm0.03}Mn_{1.02\pm0.03}Ti_{0.02\pm0.01}$	Al_6	Si_6	$(OH)_{2.47\pm0.07}O_{0.53\pm0.07}$	$F_{0.76\pm0.04}O_{0.24\pm0.04}$
S32	F-Elbaite	$Na_{0.62\pm0.01}Ca_{0.28\pm0.01}\square_{0.10\pm0.02}$	$Al_{1.19\pm0.03}Li_{0.97\pm0.04}Fe_{0.48\pm0.01}Mn_{0.34\pm0.01}Mg_{0.02\pm0.01}$	Al_6	Si_6	$(OH)_3$	$F_{0.67\pm0.03}(OH)_{0.26\pm0.04}O_{0.07\pm0.04}$

945

alkali-subgroup 3							
S33	Povondraite [a]	$Na_{0.64\pm0.03}K_{0.40\pm0.03}$	$Fe^{3+}{}_{2.41\pm0.05}Ti_{0.59\pm0.04}Cr_{0.02\pm0.01}$	$Fe^{3+}{}_{3.63\pm0.05}Mg_{1.86\pm0.02}Al_{0.47\pm0.03}$	$Si_{6.01\pm0.03}$	$(OH)_3$	$O_{0.96\pm0.03}(OH)_{0.04\pm0.03}$
alkali-subgroup 4							
S34	Darrellhenryite	$Na_{0.53\pm0.02}\square_{0.45\pm0.02}Ca_{0.01\pm0.01}$	$Al_{1.53\pm0.04}Li_{1.38\pm0.04}Mn_{0.09\pm0.01}$	Al_6	Si_6	$(OH)_{2.77\pm0.05}O_{0.24\pm0.05}$	$O_{0.60\pm0.03}F_{0.40\pm0.03}$
S35	Darrellhenryite	$Na_{0.68\pm0.02}\square_{0.30\pm0.02}Ca_{0.02\pm0.01}$	$Al_{1.20\pm0.06}Li_{1.36\pm0.05}Mn_{0.32\pm0.04}Fe_{0.11\pm0.01}$	Al_6	Si_6	$(OH)_{2.87\pm0.06}O_{0.14\pm0.06}$	$O_{0.53\pm0.04}F_{0.47\pm0.04}$
alkali-subgroup 5							
S36	F-Buergerite	$Na_{0.79\pm0.01}\square_{0.15\pm0.02}Ca_{0.05\pm0.02}$	$Fe^{3+}{}_{2.6\pm0.04}Al_{0.30\pm0.04}Ti_{0.05\pm0.01}Mg_{0.03\pm0.01}$	Al_6	$Si_{5.93\pm0.03}Al_{0.07\pm0.03}$	O_3	$F_{0.69\pm0.03}(OH)_{0.31\pm0.03}$
S37	Olenite	$Na_{0.51\pm0.01}\square_{0.46\pm0.01}Ca_{0.02\pm0.01}$	$Al_{2.91\pm0.01}Mn_{0.07\pm0.02}Fe_{0.02\pm0.01}$	Al_6	$Si_{5.87\pm0.04}Al_{0.13\pm0.04}$	O_3	$(OH)_{0.97\pm0.01}F_{0.03\pm0.01}$
calcic-subgroup 1							
S38	Uvite	$Ca_{0.41\pm0.03}Na_{0.39\pm0.02}\square_{0.21\pm0.03}$	$Mg_{2.54\pm0.02}Fe_{0.44\pm0.02}Ti_{0.03\pm0.01}$	$Al_{5.80\pm0.04}Mg_{0.20\pm0.04}$	$Si_{5.94\pm0.02}Al_{0.06\pm0.02}$	$(OH)_3$	$(OH)_{0.69\pm0.03}O_{0.20\pm0.03}F_{0.10\pm0.02}$
S39	F-Uvite	$Ca_{0.65\pm0.03}Na_{0.26\pm0.02}\square_{0.09\pm0.01}$	$Mg_{2.92\pm0.01}Ti_{0.07\pm0.01}$	$Al_{5.51\pm0.04}Mg_{0.49\pm0.04}$	Si_6	$(OH)_3$	$F_{0.55\pm0.02}(OH)_{0.36\pm0.03}O_{0.09\pm0.01}$
calcic-subgroup 2							
S40	F-Liddicoatite	$Ca_{0.59\pm0.02}Na_{0.30\pm0.01}\square_{0.11\pm0.01}$	$Li_{1.85\pm0.04}Al_{0.96\pm0.03}Fe_{0.10\pm0.02}Mn_{0.05\pm0.01}Mg_{0.05\pm0.01}$	Al_6	Si_6	$(OH)_{2.36\pm0.05}O_{0.64\pm0.05}$	$F_{0.69\pm0.03}O_{0.31\pm0.03}$
S41	F-Liddicoatite	$Ca_{0.73\pm0.05}Na_{0.21\pm0.04}\square_{0.05\pm0.02}$	$Li_{1.60\pm0.07}Al_{1.04\pm0.19}Fe_{0.16\pm0.07}Mn_{0.05\pm0.02}$	Al_6	Si_6	$(OH)_{2.74\pm0.08}O_{0.26\pm0.08}$	$F_{0.61\pm0.03}O_{0.39\pm0.03}$
S42	F-Liddicoatite	$Ca_{0.66\pm0.01}Na_{0.23\pm0.01}\square_{0.10\pm0.01}$	$Li_{1.57\pm0.04}Al_{1.37\pm0.04}Fe_{0.04\pm0.01}$	Al_6	Si_6	$(OH)_{2.80\pm0.06}O_{0.20\pm0.06}$	$F_{0.53\pm0.04}O_{0.47\pm0.04}$
calcic-subgroup 6 [b]							
S43	Adachiite	$Ca_{0.56\pm0.04}Na_{0.30\pm0.02}\square_{0.13\pm0.02}$	$Fe_{1.76\pm0.08}Mg_{0.59\pm0.03}Al_{0.55\pm0.11}Ti_{0.10\pm0.02}$	Al_6	$Si_{5.12\pm0.07}Al_{0.88\pm0.07}$	$(OH)_3$	$(OH)_{0.86\pm0.02}O_{0.13\pm0.02}$
vacant-subgroup 1							
S44	Foitite	$\square_{0.61\pm0.06}Na_{0.35\pm0.05}Ca_{0.03\pm0.02}$	$Fe_{1.28\pm0.14}Al_{1.03\pm0.05}Mn_{0.41\pm0.09}Li_{0.18\pm0.08}Mg_{0.11\pm0.07}$	Al_6	Si_6	$(OH)_3$	$(OH)_{0.93\pm0.07}F_{0.07\pm0.07}$
S45	Foitite	$\square_{0.71\pm0.02}Na_{0.28\pm0.01}$	$Fe_{1.52\pm0.03}Al_{1.04\pm0.03}Li_{0.29\pm0.04}Mn_{0.12\pm0.01}Mg_{0.01\pm0.01}$	Al_6	Si_6	$(OH)_3$	$(OH)_{0.50\pm0.47}O_{0.48\pm0.46}F_{0.02\pm0.02}$
vacant-subgroup 3							
S46	□-Fe-O root name	$\square_{0.51\pm0.04}Na_{0.48\pm0.04}$	$Fe_{1.88\pm0.04}Al_{0.99\pm0.05}Mn_{0.10\pm0.01}Mg_{0.01\pm0.01}Ti_{0.01\pm0.01}$	Al_6	$Si_{5.95\pm0.04}Al_{0.05\pm0.03}$	$(OH)_3$	$O_{0.51\pm0.04}(OH)_{0.25\pm0.03}F_{0.24\pm0.06}$

Notes: All B is assigned to the B site and assumed to be 3 apfu, Li and H_2O contents are calculated (see text). Fe and Mn are considered divalent except in sample S33 and S36, Cr is trivalent. Disorder between Y- and Z-site cations (e.g., Hawthorne 1996) is not taken into account.The prefix F- stands for fluor.

[a] chemical compositiion was determined by combined EMPA and single-crystal XRD.

[b] Number of the calcic subgroup was inferred from nomenclature in Henry et al. (2011).

946

947

948

Table 1. Chemical compositions of the studied tourmaline samples determined by electron microprobe analysis

Samples Name (IMA2011)		General tourmaline formula $XY_3Z_6(T_6O_{18})(BO_3)_3V_3W$					
		X	Y_3	Z_6	T_6	V_3	W
alkali-subgroup 1							
S1	Dravite	$Na_{0.79\pm0.01}\square_{0.12\pm0.01}Ca_{0.08\pm0.0}$	$Mg_{2.67\pm0.02}Al_{0.24\pm0.03}Fe_{0.04\pm0.01}Ti_{0.03\pm0.01}$	Al_6	Si_6	$(OH)_3$	$OH)_{0.76\pm0.02}F_{0.11\pm0.02}O_{0.12\pm0.0}$
S2	Dravite	$Na_{0.76\pm0.02}Ca_{0.13\pm0.01}\square_{0.12\pm0.0}$	$Mg_{2.71\pm0.02}Al_{0.18\pm0.02}Fe_{0.05\pm0.01}Ti_{0.04\pm0.01}$	Al_6	$Si_{6.02\pm0.01}$	$(OH)_3$	$OH)_{0.76\pm0.03}F_{0.13\pm0.02}O_{0.12\pm0.0}$
S3	Dravite	$Na_{0.61\pm0.01}\square_{0.22\pm0.02}Ca_{0.16\pm0.0}$	$Mg_{2.45\pm0.02}Al_{0.44\pm0.02}Ti_{0.05\pm0.01}Cr_{0.04\pm0.01}$	Al_6	$Si_{5.98\pm0.02}Al_{0.03\pm0.01}$	$(OH)_3$	$OH)_{0.65\pm0.02}F_{0.13\pm0.02}O_{0.22\pm0.0}$
S4	Dravite	$Na_{0.65\pm0.01}\square_{0.22\pm0.01}Ca_{0.12\pm0.0}$	$Mg_{2.26\pm0.02}Al_{0.67\pm0.02}Ti_{0.05\pm0.01}$	Al_6	$Si_{6\pm0.01}$	$(OH)_3$	$OH)_{0.66\pm0.03}F_{0.11\pm0.02}O_{0.23\pm0.0}$
S5	Dravite	$Na_{0.46\pm0.01}Ca_{0.39\pm0.01}\square_{0.13\pm0.0}$	$Mg_{2.65\pm0.01}Cr_{0.27\pm0.01}Ti_{0.03\pm0.01}$	$Al_{5.95\pm0.01}Cr_{0.05\pm0.01}$	$Si_{5.93\pm0.02}Al_{0.07\pm0.02}$	$(OH)_3$	$OH)_{0.78\pm0.02}F_{0.09\pm0.01}O_{0.13\pm0.0}$
S6	Schorl	$Na_{0.64\pm0.04}\square_{0.30\pm0.05}Ca_{0.05\pm0.0}$	$Fe_{1.88\pm0.08}Al_{0.46\pm0.1}Mg_{0.36\pm0.06}Ti_{0.03\pm0.01}$	Al_6	$Si_{5.93\pm0.03}Al_{0.07\pm0.03}$	$(OH)_3$	$OH)_{0.62\pm0.03}F_{0.07\pm0.03}O_{0.30\pm0.0}$
S7	F-Schorl	$Na_{0.68\pm0.01}\square_{0.23\pm0.02}Ca_{0.08\pm0.0}$	$Fe_{2.38\pm0.06}Al_{0.44\pm0.05}Mg_{0.09\pm0.01}Ti_{0.08\pm0.01}Mn_{0.02\pm0.01}$	Al_6	Si_6	$(OH)_3$	$F_{0.55\pm0.03}O_{0.23\pm0.02}(OH)_{0.22\pm0.0}$
S8	F-Schorl	$Na_{0.76\pm0.1}\square_{0.22\pm0.1}$	$Fe_{2.72\pm0.1}Al_{0.24\pm0.1}Mg_{0.02\pm0.01}$	Al_6	$Si_{5.93\pm0.04}Al_{0.07\pm0.03}$	$(OH)_3$	$F_{0.53\pm0.20}(OH)_{0.25\pm0.1}O_{0.22\pm0.1}$
S9	F-Schorl	$Na_{0.72\pm0.02}\square_{0.18\pm0.02}Ca_{0.10\pm0.0}$	$Fe_{2.58\pm0.06}Al_{0.61\pm0.08}Ti_{0.08\pm0.01}Mg_{0.07\pm0.01}Mn_{0.03\pm0.01}$	Al_6	Si_6	$(OH)_{2.52\pm0.08}O_{0.49\pm0.08}$	$F_{0.66\pm0.03}O_{0.35\pm0.03}$
S10	F-Schorl	$Na_{0.93\pm0.01}\square_{0.06\pm0.01}$	$Fe_{1.75\pm0.04}Al_{0.94\pm0.05}Li_{0.26\pm0.06}Ti_{0.03\pm0.01}$	Al_6	Si_6	$(OH)_{2.89\pm0.08}O_{0.11\pm0.08}$	$F_{0.79\pm0.03}O_{0.21\pm0.03}$
alkali-subgroup 2							
S11	Elbaite	$Na_{0.57\pm0.02}\square_{0.41\pm0.02}$	$Al_{1.61\pm0.05}Li_{0.91\pm0.03}Mn_{0.46\pm0.04}Ti_{0.02\pm0.01}$	Al_6	Si_6	$(OH)_3$	$OH)_{0.43\pm0.08}F_{0.26\pm0.05}O_{0.31\pm0.0}$
S12	Elbaite	$Na_{0.56\pm0.03}\square_{0.43\pm0.03}Ca_{0.02\pm0.0}$	$Al_{2.12\pm0.07}Li_{0.84\pm0.07}Mn_{0.02\pm0.01}$	Al_6	Si_6	$(OH)_3$	$OH)_{0.50\pm0.09}F_{0.24\pm0.05}O_{0.27\pm0.0}$
S13	F-Elbaite	$Na_{0.54\pm0.01}\square_{0.38\pm0.01}Ca_{0.08\pm0.0}$	$Al_{1.57\pm0.05}Li_{1.33\pm0.04}Fe_{0.06\pm0.01}Mn_{0.06\pm0.01}$	Al_6	Si_6	$(OH)_{2.74\pm0.04}O_{0.26\pm0.04}$	$F_{0.56\pm0.03}O_{0.44\pm0.03}$
S14	F-Elbaite	$Na_{0.52\pm0.01}\square_{0.43\pm0.01}Ca_{0.05\pm0.0}$	$Al_{2.06\pm0.03}Li_{0.91\pm0.06}Mn_{0.03\pm0.01}$	Al_6	Si_6	$(OH)_3$	$F_{0.35\pm0.02}O_{0.35\pm0.03}(OH)_{0.31\pm0.0}$
S15	F-Elbaite	$Na_{0.83\pm0.01}\square_{0.09\pm0.01}Ca_{0.08\pm0.0}$	$1.47\pm0.03Mn_{0.71\pm0.02}Li_{0.44\pm0.04}Fe_{0.33\pm0.02}Mg_{0.03\pm0.01}Ti_{0.03\pm0}$	Al_6	Si_6	$(OH)_{2.74\pm0.06}O_{0.26\pm0.06}$	$F_{0.73\pm0.04}O_{0.27\pm0.04}$
S16	F-Elbaite	$Na_{0.63\pm0.01}\square_{0.29\pm0.01}Ca_{0.08\pm0.0}$	$Al_{1.85\pm0.05}Li_{0.78\pm0.04}Mn_{0.36\pm0.03}$	Al_6	Si_6	$(OH)_3$	$F_{0.49\pm0.03}(OH)_{0.44\pm0.05}O_{0.07\pm0.0}$
S17	F-Elbaite	$Na_{0.66\pm0.04}\square_{0.31\pm0.05}Ca_{0.04\pm0.0}$	$Al_{1.67\pm0.09}Li_{1.06\pm0.06}Mn_{0.26\pm0.11}$	Al_6	Si_6	$(OH)_3$	$F_{0.47\pm0.06}O_{0.37\pm0.09}(OH)_{0.16\pm0.0}$
S18	F-Elbaite	$Na_{0.73\pm0.02}\square_{0.22\pm0.01}Ca_{0.05\pm0.0}$	$Al_{1.45\pm0.06}Li_{1.01\pm0.05}Fe_{0.36\pm0.03}Mn_{0.18\pm0.03}$	Al_6	Si_6	$(OH)_3$	$F_{0.67\pm0.02}O_{0.23\pm0.05}(OH)_{0.10\pm0.0}$
S19	F-Elbaite	$Na_{0.80\pm0.01}\square_{0.16\pm0.01}Ca_{0.03\pm0.0}$	$Al_{1.25\pm0.04}Li_{1.01\pm0.04}Fe_{0.50\pm0.01}Mn_{0.22\pm0.01}$	Al_6	Si_6	$(OH)_3$	$F_{0.72\pm0.03}O_{0.17\pm0.04}(OH)_{0.11\pm0.0}$
S20	F-Elbaite	$Na_{0.69\pm0.02}Ca_{0.17\pm0.05}\square_{0.14\pm0.0}$	$Al_{1.35\pm0.1}Li_{1.09\pm0.09}Mn_{0.37\pm0.02}Fe_{0.16\pm0.01}Mg_{0.02\pm0.01}$	Al_6	Si_6	$(OH)_{2.92\pm0.07}O_{0.09\pm0.07}$	$F_{0.86\pm0.05}O_{0.14\pm0.06}$
S21	F-Elbaite	$Na_{0.52\pm0.02}\square_{0.28\pm0.02}Ca_{0.20\pm0.0}$	$Al_{1.67\pm0.05}Li_{1.20\pm0.05}Mn_{0.13\pm0.01}$	Al_6	Si_6	$(OH)_{2.89\pm0.07}O_{0.11\pm0.07}$	$F_{0.63\pm0.03}O_{0.37\pm0.03}$
S22	F-Elbaite	$Na_{0.48\pm0.02}Ca_{0.26\pm0.05}\square_{0.26\pm0.0}$	$Al_{1.91\pm0.07}Li_{0.97\pm0.08}Mn_{0.11\pm0.01}$	Al_6	Si_6	$(OH)_3$	$F_{0.61\pm0.04}O_{0.24\pm0.10}(OH)_{0.16\pm0.0}$
S23	F-Elbaite	$Na_{0.54\pm0.01}\square_{0.30\pm0.05}Ca_{0.16\pm0.0}$	$Al_{1.80\pm0.13}Li_{1.01\pm0.07}Mn_{0.17\pm0.09}$	Al_6	Si_6	$(OH)_{3\pm0.04}$	$F_{0.60\pm0.05}O_{0.30\pm0.06}(OH)_{0.10\pm0.0}$
S24	F-Elbaite	$Na_{0.57\pm0.02}\square_{0.38\pm0.02}Ca_{0.05\pm0.0}$	$Al_{1.50\pm0.03}Li_{1.43\pm0.03}Mn_{0.05\pm0.01}$	Al_6	Si_6	$(OH)_{2.60\pm0.06}O_{0.40\pm0.05}$	$F_{0.59\pm0.03}O_{0.41\pm0.03}$
S25	F-Elbaite	$Na_{0.49\pm0.01}Ca_{0.26\pm0.02}\square_{0.25\pm0.0}$	$Al_{1.62\pm0.06}Li_{1.36\pm0.06}Mn_{0.02\pm0.01}$	Al_6	Si_6	$(OH)_{2.76\pm0.07}O_{0.26\pm0.07}$	$F_{0.63\pm0.03}O_{0.37\pm0.03}$
S26	F-Elbaite	$Na_{0.67\pm0.03}\square_{0.19\pm0.02}Ca_{0.13\pm0.0}$	$0.85\pm0.04Li_{1.40\pm0.04}Fe_{0.37\pm0.04}Mg_{0.32\pm0.05}Mn_{0.05\pm0.02}Ti_{0.02\pm0}$	Al_6	Si_6	$(OH)_{2.89\pm0.05}O_{0.11\pm0.05}$	$F_{0.52\pm0.06}O_{0.48\pm0.06}$
S27	F-Elbaite	$Na_{0.86\pm0.01}\square_{0.09\pm0.01}Ca_{0.06\pm0.0}$	$1.09\pm0.04Li_{0.91\pm0.04}Fe_{0.74\pm0.02}Mn_{0.22\pm0.02}Mg_{0.03\pm0.01}Ti_{0.02\pm0}$	Al_6	Si_6	$(OH)_{2.65\pm0.05}O_{0.35\pm0.05}$	$F_{0.79\pm0.03}O_{0.21\pm0.05}$
S28	F-Elbaite	$Na_{0.77\pm0.01}\square_{0.19\pm0.01}Ca_{0.04\pm0.0}$	$Al_{1.38\pm0.03}Li_{0.82\pm0.04}Fe_{0.55\pm0.01}Mn_{0.15\pm0.01}Mg_{0.10\pm0.01}$	Al_6	Si_6	$(OH)_{2.77\pm0.3}O_{0.23\pm0.3}$	$F_{0.65\pm0.03}(OH)_{0.21\pm0.16}O_{0.15\pm0.1}$
S29	F-Elbaite	$Na_{0.77\pm0.01}\square_{0.20\pm0.01}Ca_{0.03\pm0.0}$	$Al_{1.27\pm0.02}Li_{0.92\pm0.03}Fe_{0.58\pm0.01}Mn_{0.22\pm0.02}$	Al_6	Si_6	$(OH)_3$	$F_{0.58\pm0.03}(OH)_{0.29\pm0.05}O_{0.13\pm0.0}$
S30	F-Elbaite	$Na_{0.65\pm0.01}Ca_{0.25\pm0.01}\square_{0.09\pm0.0}$	$Al_{1.31\pm0.03}Li_{1.05\pm0.03}Mn_{0.61\pm0.02}Ti_{0.03\pm0.01}$	Al_6	Si_6	$(OH)_3$	$F_{0.58\pm0.04}O_{0.14\pm0.04}(OH)_{0.07\pm0.0}$
S31	F-Elbaite	$Na_{0.86\pm0.01}\square_{0.09\pm0.02}Ca_{0.05\pm0.0}$	$Al_{1.27\pm0.03}Li_{0.69\pm0.03}Mn_{1.02\pm0.03}Ti_{0.02\pm0.01}$	Al_6	Si_6	$(OH)_{2.47\pm0.07}O_{0.53\pm0.07}$	$F_{0.76\pm0.04}O_{0.24\pm0.04}$
S32	F-Elbaite	$Na_{0.62\pm0.01}Ca_{0.28\pm0.01}\square_{0.10\pm0.0}$	$Al_{1.19\pm0.03}Li_{0.97\pm0.04}Fe_{0.48\pm0.01}Mn_{0.34\pm0.01}Mg_{0.02\pm0.01}$	Al_6	Si_6	$(OH)_3$	$F_{0.67\pm0.03}(OH)_{0.26\pm0.04}O_{0.07\pm0.0}$

alkali-subgroup 3							
S33	Povondraite [a]	$Na_{0.64\pm0.03}K_{0.40\pm0.03}$	$Fe^{3+}_{2.41\pm0.05}Ti_{0.59\pm0.04}Cr_{0.02\pm0.01}$	$e^{3+}_{3.63\pm0.05}Mg_{1.86\pm0.02}Al_{0.47\pm0.}$	$Si_{6.01\pm0.03}$	$(OH)_3$	$O_{0.96\pm0.03}(OH)_{0.04\pm0.03}$
alkali-subgroup 4							
S34	Darrellhenryite	$Na_{0.53\pm0.02}\square_{0.45\pm0.02}Ca_{0.01\pm0.0}$	$Al_{1.53\pm0.04}Li_{1.38\pm0.04}Mn_{0.09\pm0.01}$	Al_6	Si_6	$(OH)_{2.77\pm0.05}O_{0.24\pm0.05}$	$O_{0.60\pm0.03}F_{0.40\pm0.03}$
S35	Darrellhenryite	$Na_{0.68\pm0.02}\square_{0.30\pm0.02}Ca_{0.02\pm0.0}$	$Al_{1.20\pm0.06}Li_{1.36\pm0.05}Mn_{0.32\pm0.04}Fe_{0.11\pm0.01}$	Al_6	Si_6	$(OH)_{2.87\pm0.06}O_{0.14\pm0.06}$	$O_{0.53\pm0.04}F_{0.47\pm0.04}$
alkali-subgroup 5							
S36	F-Buergerite	$Na_{0.79\pm0.01}\square_{0.15\pm0.02}Ca_{0.05\pm0.0}$	$Fe^{3+}_{2.6+0.04}Al_{0.30+0.04}Ti_{0.05+0.01}Mg_{0.03+0.01}$	Al_6	$Si_{5.93\pm0.03}Al_{0.07\pm0.03}$	O_3	$F_{0.69\pm0.03}(OH)_{0.31\pm0.03}$
S37	Olenite	$Na_{0.51\pm0.01}\square_{0.46\pm0.01}Ca_{0.02\pm0.0}$	$Al_{2.91\pm0.01}Mn_{0.07\pm0.02}Fe_{0.02\pm0.01}$	Al_6	$Si_{5.87\pm0.04}Al_{0.13\pm0.04}$	O_3	$(OH)_{0.97\pm0.01}F_{0.03\pm0.01}$
calcic-subgroup 1							
S38	Uvite	$Ca_{0.41\pm0.03}Na_{0.39\pm0.02}\square_{0.21\pm0.0}$	$Mg_{2.54\pm0.02}Fe_{0.44\pm0.02}Ti_{0.03\pm0.01}$	$Al_{5.80\pm0.04}Mg_{0.20\pm0.04}$	$Si_{5.94\pm0.02}Al_{0.06\pm0.02}$	$(OH)_3$	$(OH)_{0.69\pm0.03}O_{0.20\pm0.03}F_{0.10\pm0.0}$
S39	F-Uvite	$Ca_{0.65\pm0.03}Na_{0.26\pm0.02}\square_{0.09\pm0.0}$	$Mg_{2.92\pm0.01}Ti_{0.07\pm0.01}$	$Al_{5.51\pm0.04}Mg_{0.49\pm0.04}$	Si_6	$(OH)_3$	$F_{0.55\pm0.02}(OH)_{0.36\pm0.03}O_{0.09\pm0.0}$
calcic-subgroup 2							
S40	F-Liddicoatite	$Ca_{0.59\pm0.02}Na_{0.30\pm0.01}\square_{0.11\pm0.0}$	$Li_{1.85\pm0.04}Al_{0.96\pm0.03}Fe_{0.10\pm0.02}Mn_{0.05\pm0.01}Mg_{0.05\pm0.01}$	Al_6	Si_6	$(OH)_{2.36\pm0.05}O_{0.64\pm0.05}$	$F_{0.69\pm0.03}O_{0.31\pm0.03}$
S41	F-Liddicoatite	$Ca_{0.73\pm0.05}Na_{0.21\pm0.04}\square_{0.05\pm0.0}$	$Li_{1.60\pm0.07}Al_{1.04\pm0.19}Fe_{0.16\pm0.07}Mn_{0.05\pm0.02}$	Al_6	Si_6	$(OH)_{2.74\pm0.08}O_{0.26\pm0.08}$	$F_{0.61\pm0.03}O_{0.39\pm0.03}$
S42	F-Liddicoatite	$Ca_{0.66\pm0.01}Na_{0.23\pm0.01}\square_{0.10\pm0.0}$	$Li_{1.57\pm0.04}Al_{1.37\pm0.04}Fe_{0.04\pm0.01}$	Al_6	Si_6	$(OH)_{2.80\pm0.06}O_{0.20\pm0.06}$	$F_{0.53\pm0.04}O_{0.47\pm0.04}$
calcic-subgroup 6 [b]							
S43	Adachiite	$Ca_{0.56\pm0.04}Na_{0.30\pm0.02}\square_{0.13\pm0.0}$	$Fe_{1.76\pm0.08}Mg_{0.59\pm0.03}Al_{0.55\pm0.11}Ti_{0.10\pm0.02}$	Al_6	$Si_{5.12\pm0.07}Al_{0.88\pm0.07}$	$(OH)_3$	$(OH)_{0.86\pm0.02}O_{0.13\pm0.02}$
vacant-subgroup 1							
S44	Foitite	$\square_{0.61\pm0.06}Na_{0.35\pm0.05}Ca_{0.03\pm0.0}$	$Fe_{1.28\pm0.14}Al_{1.03\pm0.05}Mn_{0.41\pm0.09}Li_{0.18\pm0.08}Mg_{0.11\pm0.07}$	Al_6	Si_6	$(OH)_3$	$(OH)_{0.93\pm0.07}F_{0.07\pm0.07}$
S45	Foitite	$\square_{0.71\pm0.02}Na_{0.28\pm0.01}$	$Fe_{1.52\pm0.03}Al_{1.04\pm0.03}Li_{0.29\pm0.04}Mn_{0.12\pm0.01}Mg_{0.01\pm0.01}$	Al_6	Si_6	$(OH)_3$	$(OH)_{0.50\pm0.47}O_{0.48\pm0.46}F_{0.02\pm0.0}$
vacant-subgroup 3							
S46	□-Fe-O root nam	$\square_{0.51\pm0.04}Na_{0.48\pm0.04}$	$Fe_{1.88\pm0.04}Al_{0.99\pm0.05}Mn_{0.10\pm0.01}Mg_{0.01\pm0.01}Ti_{0.01\pm0.01}$	Al_6	$Si_{5.95\pm0.04}Al_{0.05\pm0.03}$	$(OH)_3$	$O_{0.51\pm0.04}(OH)_{0.25\pm0.03}F_{0.24\pm0.0}$

Notes: All B is assigned to the B site and assumed to be 3 apfu, Li and H_2O contents are calculated (see text). Fe and Mn are considered divalent except in sample S33 and S36, Cr is trivalent. Disorder between Y- and Z-site cations (e.g., Hawthorne 1996) is not taken into account. The prefix F- stands for fluor.

[a] chemical compositiion was determined by combined EMPA and single-crystal XRD.

[b] Number of the calcic subgroup was inferred from nomenclature in Henry et al. (2011).

Table 2. Tourmaline sites with respective symmetry, Wyckoff position and Raman-active phonon modes in five scattering geometries. Out of $32A_1$+ 54E phonon modes in total, there are $31A_1$+ 53E optical and A_1 + E acoustic modes. Only optical modes are Raman-active

Site	**Wykoff position**	**Site symmetry**	**Raman-active phonon modes**				
			$\bar{y}(zz)y$	$\bar{y}(xz)y$	$\bar{y}(xx)y$	$\bar{z}(xx)z$	$\bar{z}(xy)z$
X	3a	3m	A1 (T)	E (T)	A1 (T) + E (L)	A1 (L) + E (T)	E (T)
Y	9b	.m	2A1 (T)	3E (T)	2A1 (T) + 3E (L)	2A1 (L) + 3E (T)	3E (T)
Z	18c	1	3A1 (T)	6E (T)	3A1 (T) + 6E (L)	3A1 (L) + 6E (T)	6E (T)
T	18c	1	3A1 (T)	6E (T)	3A1 (T) + 6E (L)	3A1 (L) + 6E (T)	6E (T)
B	9b	.m	2A1 (T)	3E (T)	2A1 (T) + 3E (L)	2A1 (L) + 3E (T)	3E (T)
O1	3a	3m	A1 (T)	E (T)	A1 (T) + E (L)	A1 (L) + E (T)	E (T)
O2	9b	.m	2A1 (T)	3E (T)	2A1 (T) + 3E (L)	2A1 (L) + 3E (T)	3E (T)
O3	9b	.m	2A1 (T)	3E (T)	2A1 (T) + 3E (L)	2A1 (L) + 3E (T)	3E (T)
O4	9b	.m	2A1 (T)	3E (T)	2A1 (T) + 3E (L)	2A1 (L) + 3E (T)	3E (T)
O5	9b	.m	2A1 (T)	3E (T)	2A1 (T) + 3E (L)	2A1 (L) + 3E (T)	3E (T)
O6	18c	1	3A1 (T)	6E (T)	3A1 (T) + 6E (L)	3A1 (L) + 6E (T)	6E (T)
O7	18c	1	3A1 (T)	6E (T)	3A1 (T) + 6E (L)	3A1 (L) + 6E (T)	6E (T)
O8	18c	1	3A1 (T)	6E (T)	3A1 (T) + 6E (L)	3A1 (L) + 6E (T)	6E (T)
H1	3a	3m	A1 (T)	E (T)	A1 (T) + E (L)	A1 (L) + E (T)	E (T)
H2	9b	.m	2A1 (T)	3E (T)	2A1 (T) + 3E (L)	2A1 (L) + 3E (T)	3E (T)

Notes: T refers transverse, L to longitudinal.

Table 3. Averaged Raman frequencies (cm^{-1}) of assigned ^{V}OH and ^{W}OH stretching modes

Species	^{V}OH modes					
Dravite		$^{Y}Mg^{Z}Al^{Z}Al$-$2^{Y}Al^{Z}Al^{Z}Al$		$2^{Y}Mg^{Z}Al^{Z}Al$-$^{Y}Al^{Z}Al^{Z}Al$	$3^{Y}Mg^{Z}Al^{Z}Al$	
		3494 ± 8		3534 ± 7	3573 ± 4	
Schorl		$^{Y}Fe^{Z}Al^{Z}Al$-$2^{Y}Al^{Z}Al^{Z}Al$		$2^{Y}Fe^{Z}Al^{Z}Al$-$^{Y}Al^{Z}Al^{Z}Al$	$3^{Y}Fe^{Z}Al^{Z}Al$	
		3500 ± 3		3545 ± 2	3566 ± 1	
Elbaite[a]	$^{Y}Fe^{*Z}Al^{Z}Al$-$2^{Y}Al^{Z}Al^{Z}Al$	$^{Y}Li^{Z}Al^{Z}Al$-$2^{Y}Al^{Z}Al^{Z}Al$	$2^{Y}Fe^{*Z}Al^{Z}Al$-$^{Y}Al^{Z}Al^{Z}Al$	$2^{Y}Li^{Z}Al^{Z}Al$-$^{Y}Al^{Z}Al^{Z}Al$		
	3465 ± 11	3494 ± 8	3562 ± 4	3593 ± 4		
Povondraite				$2^{Y}(Fe^{3+})^{Z}(Fe^{3+})^{Z}Mg$-$^{Y}(Fe^{3+})^{Z}(Fe^{3+})^{Z}(Fe^{3+})$	$3^{Y}(Fe^{3+})^{Z}(Fe^{3+})^{Z}Mg$	
				3554±1	3596±2	
Fluor-buergerite				$2^{Y}(Fe^{3+})^{Z}Al^{Z}Al$-$^{Y}Al^{Z}Al^{Z}Al$	$3^{Y}(Fe^{3+})^{Z}Al^{Z}Al$	
				3490 ± 2	3531 ± 1	
Olenite	$3^{Y}Al^{Z}Al$-$^{X}\square$	$^{Y}Fe^{*Z}Al^{Z}Al$-$2^{Y}Al^{Z}Al^{Z}Al$+ $^{Y}Li^{Z}Al^{Z}Al$-$2^{Y}Al^{Z}Al^{Z}Al$	$2^{Y}Fe^{*Z}Al^{Z}Al$-$^{Y}Al^{Z}Al^{Z}Al$	$2^{Y}Li^{Z}Al^{Z}Al$-$^{Y}Al^{Z}Al^{Z}Al$		
	3455 ± 1	3504 ± 4	3562 ± 7	3592 ± 1		
Uvite	3MgAlAl-$^{X}\square$	MgMgAl-2MgAlAl		2MgMgAl-MgAlAl	3MgMgAl	
	3485 ± 5	3518 ± 3		3547 ± 2	3579 ± 2	
Fluor-liddicoatite	$3^{Y}Al^{Z}Al^{Z}Al$-$^{X}\square$	$^{Y}Li^{Z}Al^{Z}Al$-$2^{Y}Al^{Z}Al^{Z}Al$	$^{Y}Li^{Z}Al^{Z}Al$-$^{Y}Fe^{*Z}Al^{Z}Al$-$^{Y}Al^{Z}Al^{Z}Al$	$2^{Y}Li^{Z}Al^{Z}Al$-$^{Y}Al^{Z}Al^{Z}Al$	$3^{Y}Li^{Z}Al^{Z}Al$	
	3475 ± 9	3511 ± 3	3551 ± 6	3582 ± 3	3607 ± 1	
Adachiite				$2^{Y}Fe^{Z}Al^{Z}Al$-$^{Y}Al^{Z}Al^{Z}Al$	$3^{Y}Fe^{Z}Al^{Z}Al$	$3^{Y}Mg^{Z}Al^{Z}Al$
				3486 ± 2	3527 ± 1	3565 ± 1
Foitite[b]		$^{Y}Fe^{*Z}Al^{Z}Al$-$2^{Y}Al^{Z}Al^{Z}Al$	$^{Y}Li^{Z}Al^{Z}Al$-$2^{Y}Al^{Z}Al^{Z}Al$ [c]	$2^{Y}Fe^{*Z}Al^{Z}Al$-$^{Y}Al^{Z}Al^{Z}Al$	$3^{Y}Fe^{Z}Al^{Z}Al$	
		3484 ± 6	3517 ± 2	3551 ± 1	3570 ± 3	

Species	^{W}OH modes				
Dravite	$^{Y}Mg^{Y}Al$-$^{X}\square$	$^{Y}Mg^{Y}Mg^{Y}Al$-$^{X}\square$		$^{Y}Mg^{Y}Mg^{Y}Al$-^{X}Na	$^{Y}Mg^{Y}Mg^{Y}Mg$-^{X}(Na+Ca)
	3639 ± 3	3668 ± 1		3739 ± 2	3770 ± 2
Schorl	$^{Y}Fe^{Y}Al^{Y}Al$-$^{X}\square$			$^{Y}Fe^{Y}Fe^{Y}Al$-^{X}Na	
	3630 ± 1			3720 ± 2	
Elbaite[a]	$^{Y}Li^{Y}Al^{Y}Al$-$^{X}\square$		$^{Y}Li^{Y}$(Li,Fe*)^{Y}Al-$^{X}\square$ [c]	$^{Y}Li^{Y}Al^{Y}Al$-^{X}Na	
	3652 ± 2		3678 ± 4	3714 ± 2	
Olenite	$^{Y}Li^{Y}Al^{Y}Al$-$^{X}\square$				
	3652 ± 2				
Uvite	$^{Y}Mg^{Y}Al^{Y}Al$-$^{X}\square$	$^{Y}Mg^{Y}Mg^{Y}Al$-$^{X}\square$		$^{Y}Mg^{Y}Mg^{Y}Al$-^{X}Na	$^{Y}Mg^{Y}Mg^{Y}Mg$-^{X}(Na+Ca)
	3639 ± 3	3668 ± 1		3740 ± 3	3769 ± 1
Fluor-liddicoatite	$^{Y}Li^{Y}Al^{Y}Al$-$^{X}\square$				
	3652 ± 3				
Adachiite		$^{Y}Fe^{Y}Fe^{Y}Al$-$^{X}\square$		$^{Y}Fe^{Y}Fe^{Y}Al$-^{X}Na + $^{Y}Mg^{Y}Mg^{Y}Al$-^{X}Na	
		3625 ± 1		3679 ± 1	
Foitite[b]	$^{Y}Fe^{*Y}Al^{Y}Al$-$^{X}\square$	$^{Y}Fe^{*Y}Fe^{*Y}Al$-$^{X}\square$	$^{Y}Li^{Y}Fe^{*Y}Al$-$^{X}\square$ [c]	$^{Y}Fe^{*Y}Fe^{*Y}Al$-^{X}Na	
	3631 ± 1	3644 ± 1	3670 ± 1	3726 ± 1	

Notes: Fluor-species are included in the averages. Except for povondraite and F-buergerite, Fe and Mn are always considered divalent and Fe* = (Fe^{2+}+Mn^{2+}). Statistical errors are given for the frequencies except for povondraite, Fluor-buergerite, olenite and adachiite for which relative errors from data fitting are shown.

[a] data of the darrellhenryite samples are included in the averaged frequencies of elbaite, because of the same band assignment.

[b] data of the □-Fe-O root name sample are included in the averaged frequencies of foitite, because of the same band assignment.

[c] modes are only observed in (Fe,Mn)-bearing elbaite depending on the Li and Fe* content and Li-bearing foitite.

Table 4. Linear equations (general formula (cm^{-1}) = a *x* (apfu) + b) of the fitted peak position of selected ^{V}OH vibrational modes shown in figures 9 ,10, and 11

vib. mode / element content	^{X}(Na+Ca)	^{X}Na/^{X}(Na+Ca)
$3^{Y}Mg^{Z}Al^{Z}Al$	(30±12)*x* + (3547±10)	(31±28)*x* + (3546±24)
$2^{Y}Mg^{Z}Al^{Z}Al$-$^{Y}Al^{Z}Al^{Z}Al$	(104±44)*x* + (3447±37)	(106±83)*x* + (3444±70)
$^{Y}Mg^{Z}Al^{Z}Al$-$2^{Y}Al^{Z}Al^{Z}Al$	(100±53)*x* + (3413±45)	–
$3^{Y}Fe^{*Z}Al^{Z}Al$	(22±3)*x* + (3562±1) [a]	–
$2^{Y}Fe^{*Z}Al^{Z}Al$-$^{Y}Al^{Z}Al^{Z}Al$	(16±3)*x* + (3545±1) [a]	–
$^{Y}Fe^{*Z}Al^{Z}Al$-$2^{Y}Al^{Z}Al^{Z}Al$	(41±3)*x* + (3467±2)	–
$2^{Y}Li^{Z}Al^{Z}Al$-$^{Y}Al^{Z}Al^{Z}Al$	(22±6)*x* + (3576±4)	(58±3)*x* + (3565.9±0.6) [b]
$^{Y}Li^{Z}Al^{Z}Al$-$2^{Y}Al^{Z}Al^{Z}Al$	(39±15)*x* + (3467±11)	(-23±5)*x* + (3519±4)

[a] linear trends of the data points of foitite.

[b] linear trends of the data points of liddicoatite.

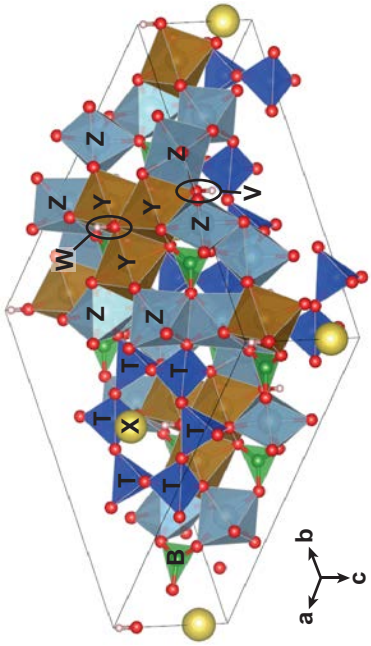

Figure 1

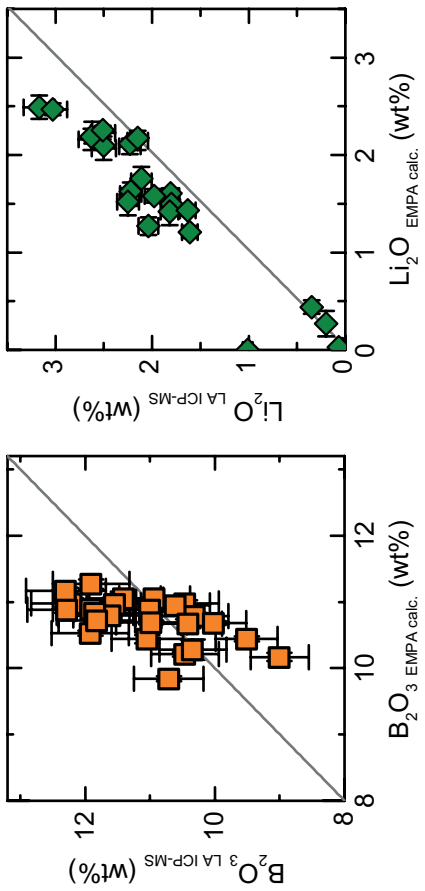
Li_2O EMPA calc. (wt%)
Li_2O LA ICP-MS (wt%)
0
1
2
3
B_2O_3 EMPA calc. (wt%)
B_2O_3 LA ICP-MS (wt%)
8
10
12

Figure 2

Figure 3

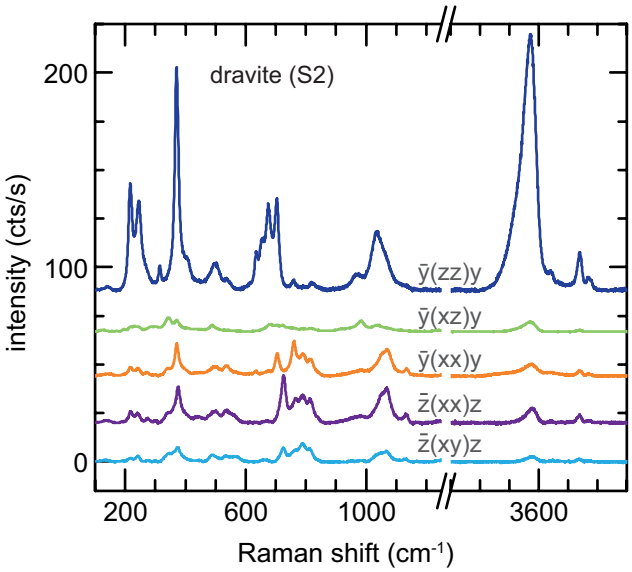
dravite (S2)
intensity (cts/s)
200
100
0
ȳ(zz)y
ȳ(xz)y
ȳ(xx)y
z̄(xx)z
z̄(xy)z
200
600
1000
3600
Raman shift (cm-1)

Figure 4

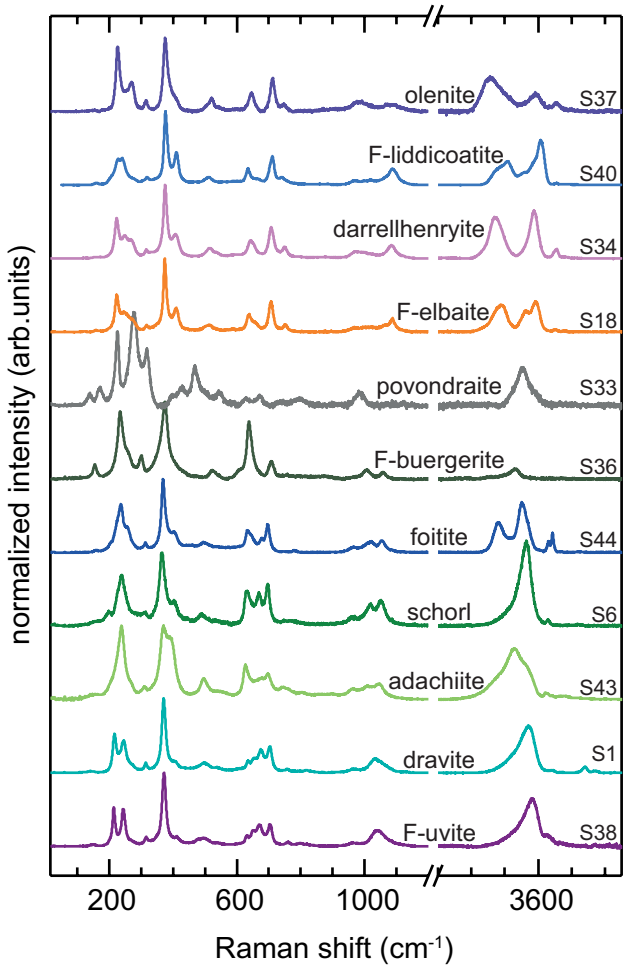
olenite
S37
F-liddicoatite
S40
darrellhenryite
S34
F-elbaite
S18
povondraite
S33
F-buergerite
S36
foitite
S44
schorl
S6
adachiite
S43
dravite
S1
F-uvite
S38
normalized intensity (arb.units)
200
600
1000
3600
Raman shift (cm-1)

Figure 5

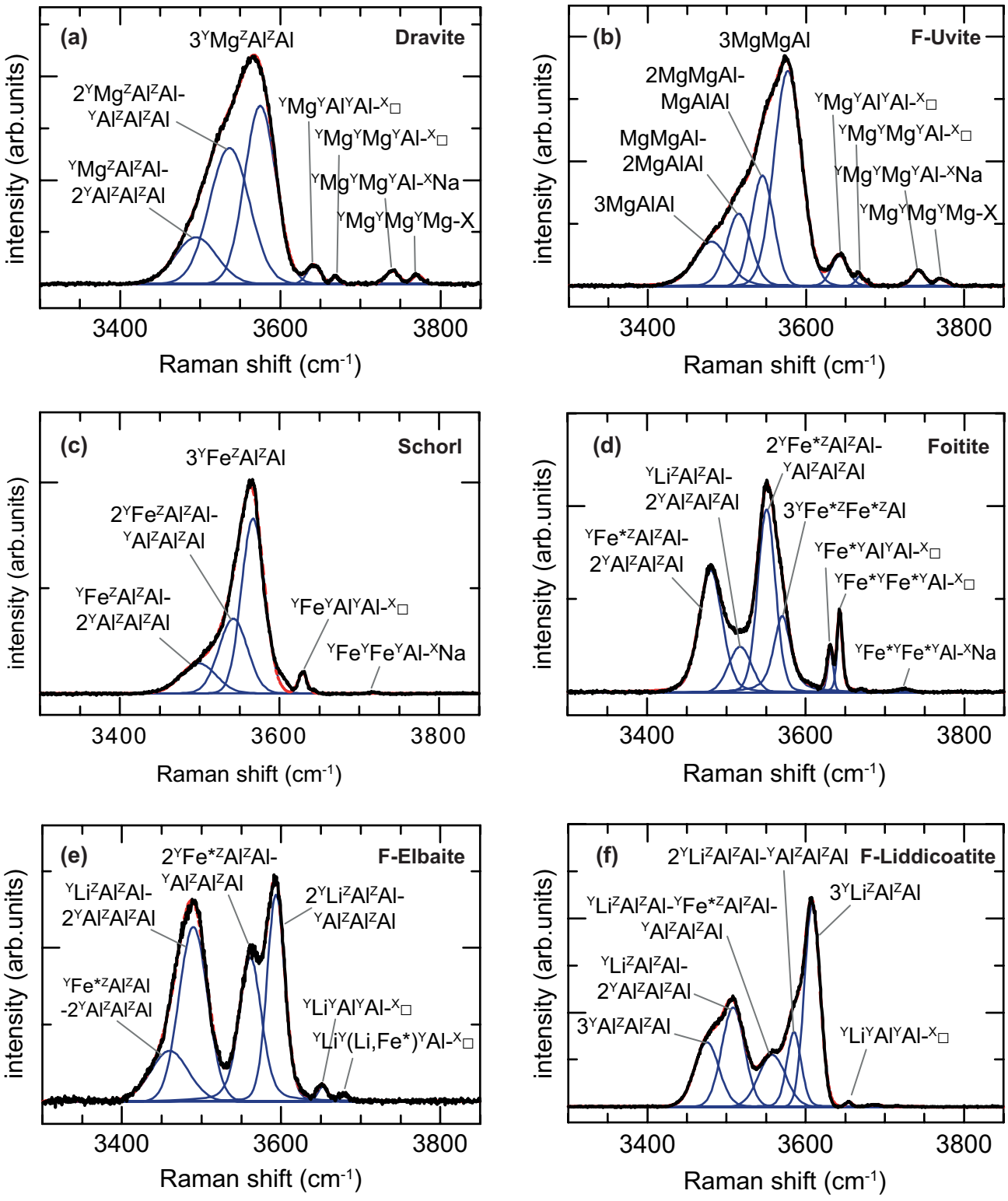
(a)
Dravite
$^{3Y}Mg^{Z}Al^{Z}Al$
$^{2Y}Mg^{Z}Al^{Z}Al$-$^{Y}Al^{Z}Al^{Z}Al$
$^{Y}Mg^{Z}Al^{Z}Al$-$^{2Y}Al^{Z}Al^{Z}Al$
$^{Y}Mg^{Y}Al^{Y}Al$-$^{X}\square$
$^{Y}Mg^{Y}Mg^{Y}Al$-$^{X}\square$
$^{Y}Mg^{Y}Mg^{Y}Al$-^{X}Na
$^{Y}Mg^{Y}Mg^{Y}Mg$-X
(b)
F-Uvite
3MgMgAl
2MgMgAl-MgAlAl
MgMgAl-2MgAlAl
3MgAlAl
$^{Y}Mg^{Y}Al^{Y}Al$-$^{X}\square$
$^{Y}Mg^{Y}Mg^{Y}Al$-$^{X}\square$
$^{Y}Mg^{Y}Mg^{Y}Al$-^{X}Na
$^{Y}Mg^{Y}Mg^{Y}Mg$-X
(c)
Schorl
$^{3Y}Fe^{Z}Al^{Z}Al$
$^{2Y}Fe^{Z}Al^{Z}Al$-$^{Y}Al^{Z}Al^{Z}Al$
$^{Y}Fe^{Z}Al^{Z}Al$-$^{2Y}Al^{Z}Al^{Z}Al$
$^{Y}Fe^{Y}Al^{Y}Al$-$^{X}\square$
$^{Y}Fe^{Y}Fe^{Y}Al$-^{X}Na
(d)
Foitite
$^{2Y}Fe^{*Z}Al^{Z}Al$-$^{Y}Al^{Z}Al^{Z}Al$
$^{Y}Li^{Z}Al^{Z}Al$-$^{2Y}Al^{Z}Al^{Z}Al$
$^{3Y}Fe^{*Z}Fe^{*Z}Al$
$^{Y}Fe^{*Z}Al^{Z}Al$-$^{2Y}Al^{Z}Al^{Z}Al$
$^{Y}Fe^{*Y}Al^{Y}Al$-$^{X}\square$
$^{Y}Fe^{*Y}Fe^{*Y}Al$-$^{X}\square$
$^{Y}Fe^{*Y}Fe^{*Y}Al$-^{X}Na
(e)
F-Elbaite
$^{2Y}Fe^{*Z}Al^{Z}Al$-$^{Y}Al^{Z}Al^{Z}Al$
$^{Y}Li^{Z}Al^{Z}Al$-$^{2Y}Al^{Z}Al^{Z}Al$
$^{2Y}Li^{Z}Al^{Z}Al$-$^{Y}Al^{Z}Al^{Z}Al$
$^{Y}Fe^{*Z}Al^{Z}Al$-$^{2Y}Al^{Z}Al^{Z}Al$
$^{Y}Li^{Y}Al^{Y}Al$-$^{X}\square$
$^{Y}Li^{Y}(Li,Fe^{*})^{Y}Al$-$^{X}\square$
(f)
F-Liddicoatite
$^{2Y}Li^{Z}Al^{Z}Al$-$^{Y}Al^{Z}Al^{Z}Al$
$^{3Y}Li^{Z}Al^{Z}Al$
$^{Y}Li^{Z}Al^{Z}Al$-$^{Y}Fe^{*Z}Al^{Z}Al$-$^{Y}Al^{Z}Al^{Z}Al$
$^{Y}Li^{Z}Al^{Z}Al$-$^{2Y}Al^{Z}Al^{Z}Al$
$^{3Y}Al^{Z}Al^{Z}Al$
$^{Y}Li^{Y}Al^{Y}Al$-$^{X}\square$
intensity (arb.units)
3400
3600
3800
Raman shift (cm^{-1})

Figure 6

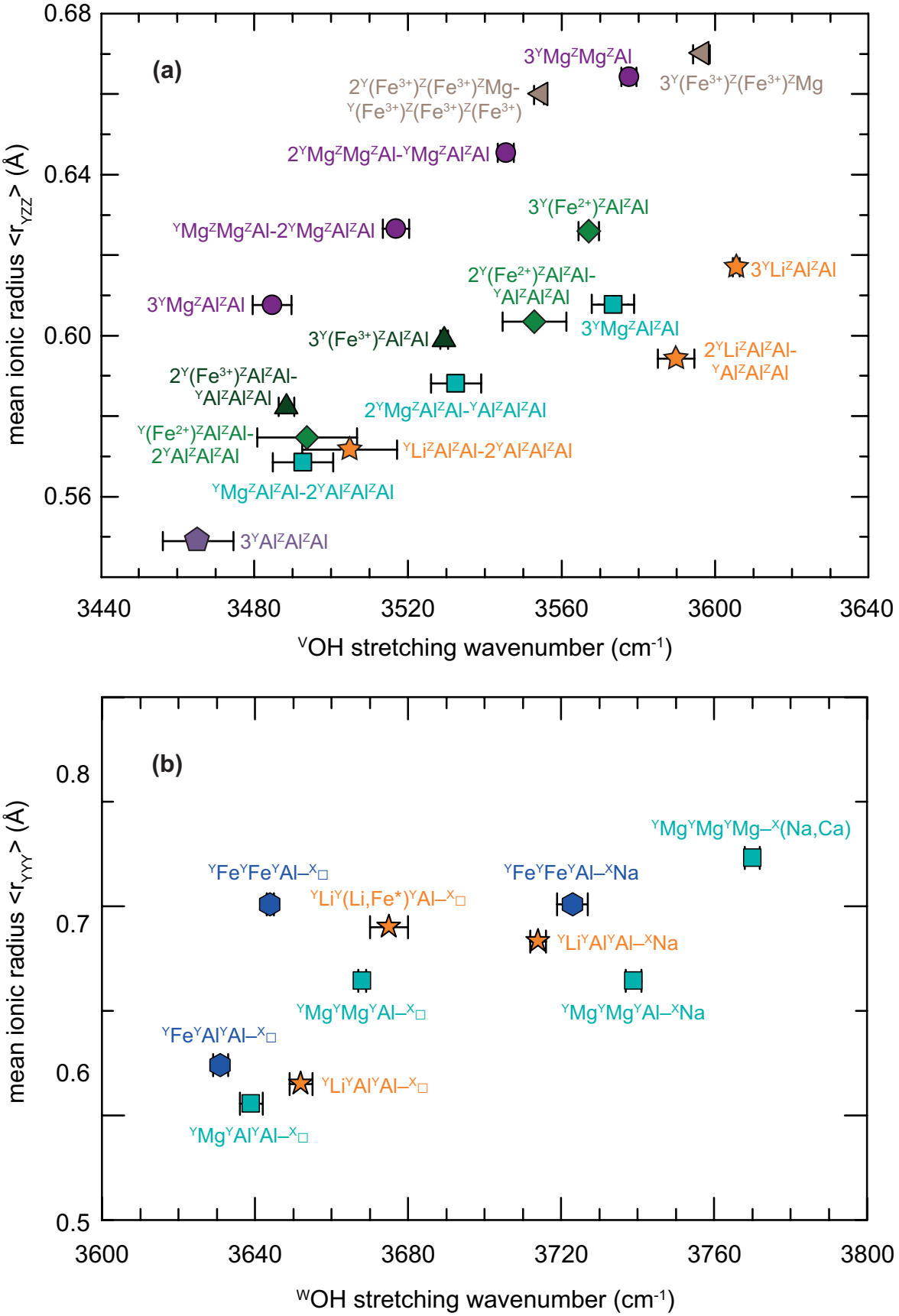
(a)
mean ionic radius <r_YZZ> (Å)
0.68
0.64
0.60
0.56
3440
3480
3520
3560
3600
3640
VOH stretching wavenumber (cm-1)
3YMgZMgZAl
3Y(Fe3+)Z(Fe3+)ZMg
2Y(Fe3+)Z(Fe3+)ZMg-Y(Fe3+)Z(Fe3+)Z(Fe3+)
2YMgZMgZAl-YMgZAlZAl
3Y(Fe2+)ZAlZAl
YMgZMgZAl-2YMgZAlZAl
3YLiZAlZAl
2Y(Fe2+)ZAlZAl-YAlZAlZAl
3YMgZAlZAl
3Y(Fe3+)ZAlZAl
3YMgZAlZAl
2YLiZAlZAl-YAlZAlZAl
2Y(Fe3+)ZAlZAl-YAlZAlZAl
2YMgZAlZAl-YAlZAlZAl
Y(Fe2+)ZAlZAl-2YAlZAlZAl
YLiZAlZAl-2YAlZAlZAl
YMgZAlZAl-2YAlZAlZAl
3YAlZAlZAl
(b)
mean ionic radius <r_YYY> (Å)
0.8
0.7
0.6
0.5
3600
3640
3680
3720
3760
3800
WOH stretching wavenumber (cm-1)
YMgYMgYMg–X(Na,Ca)
YFeYFeYAl–X□
YFeYFeYAl–XNa
YLiY(Li,Fe*)YAl–X□
YLiYAlYAl–XNa
YMgYMgYAl–X□
YMgYMgYAl–XNa
YFeYAlYAl–X□
YLiYAlYAl–X□
YMgYAlYAl–X□

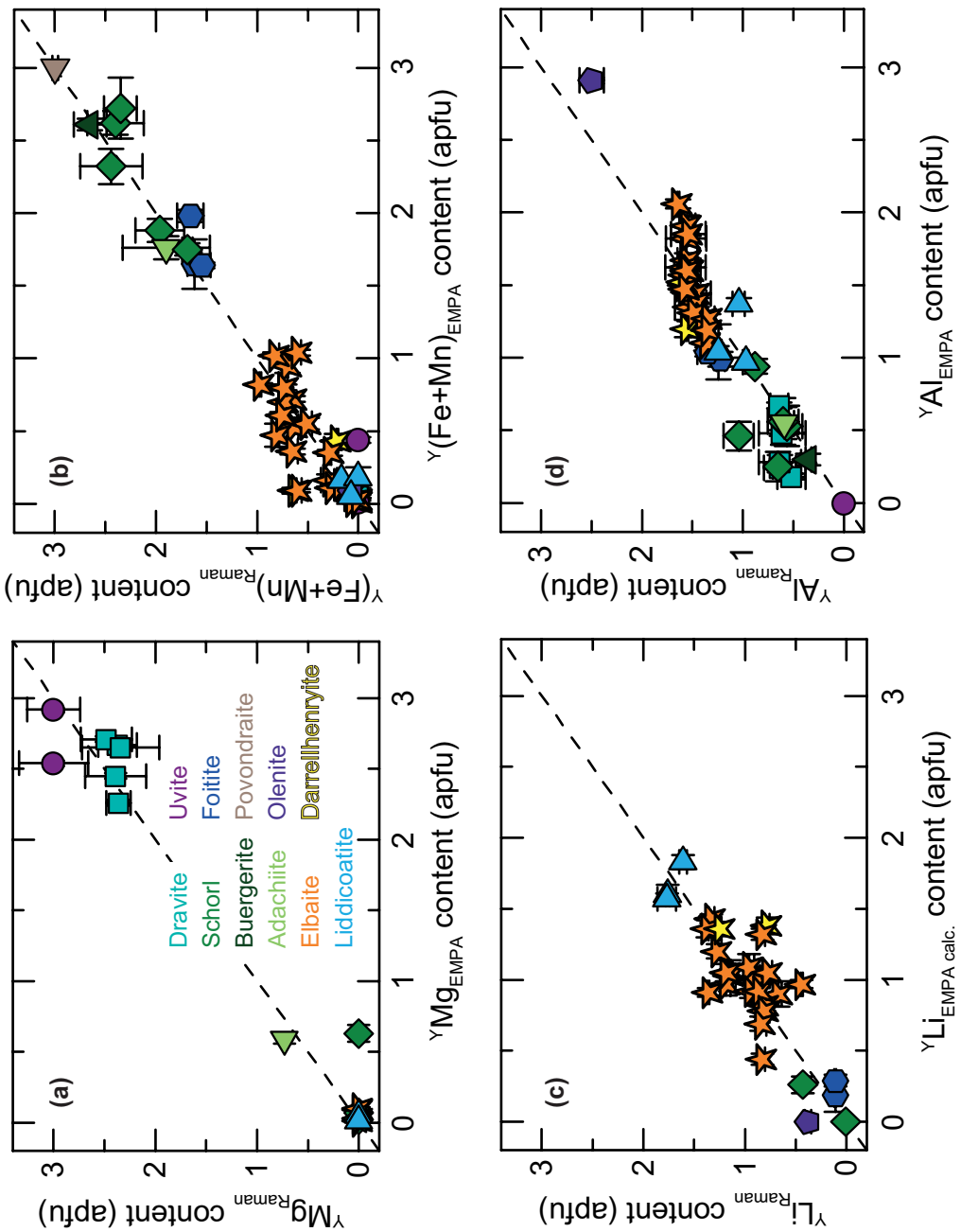
(a)
(b)
(c)
(d)
Dravite
Schorl
Buergerite
Adachiite
Elbaite
Liddicoatite
Uvite
Foitite
Povondraite
Olenite
Darrellhenryite
$^{Y}Mg_{Raman}$ content (apfu)
$^{Y}Mg_{EMPA}$ content (apfu)
$^{Y}(Fe+Mn)_{Raman}$ content (apfu)
$^{Y}(Fe+Mn)_{EMPA}$ content (apfu)
$^{Y}Li_{Raman}$ content (apfu)
$^{Y}Li_{EMPA\ calc.}$ content (apfu)
$^{Y}Al_{Raman}$ content (apfu)
$^{Y}Al_{EMPA}$ content (apfu)

Figure 7

Figure 8

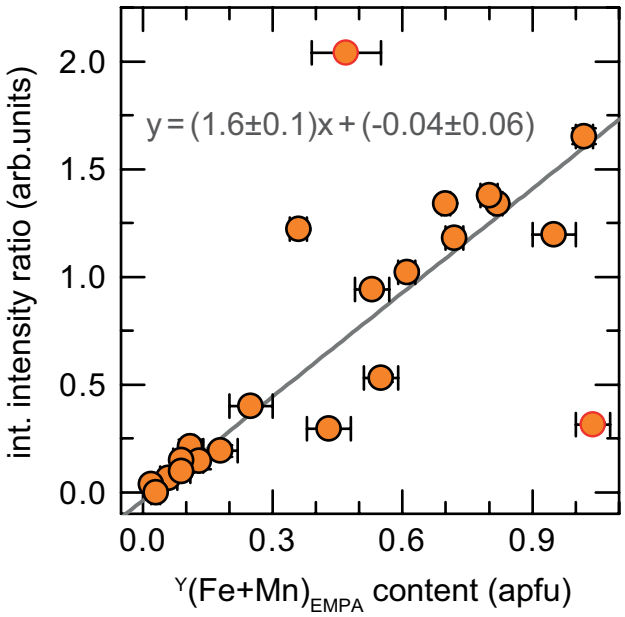
y = (1.6±0.1)x + (-0.04±0.06)
int. intensity ratio (arb.units)
2.0
1.5
1.0
0.5
0.0
0.0
0.3
0.6
0.9
Y(Fe+Mn)EMPA content (apfu)

Figure 9

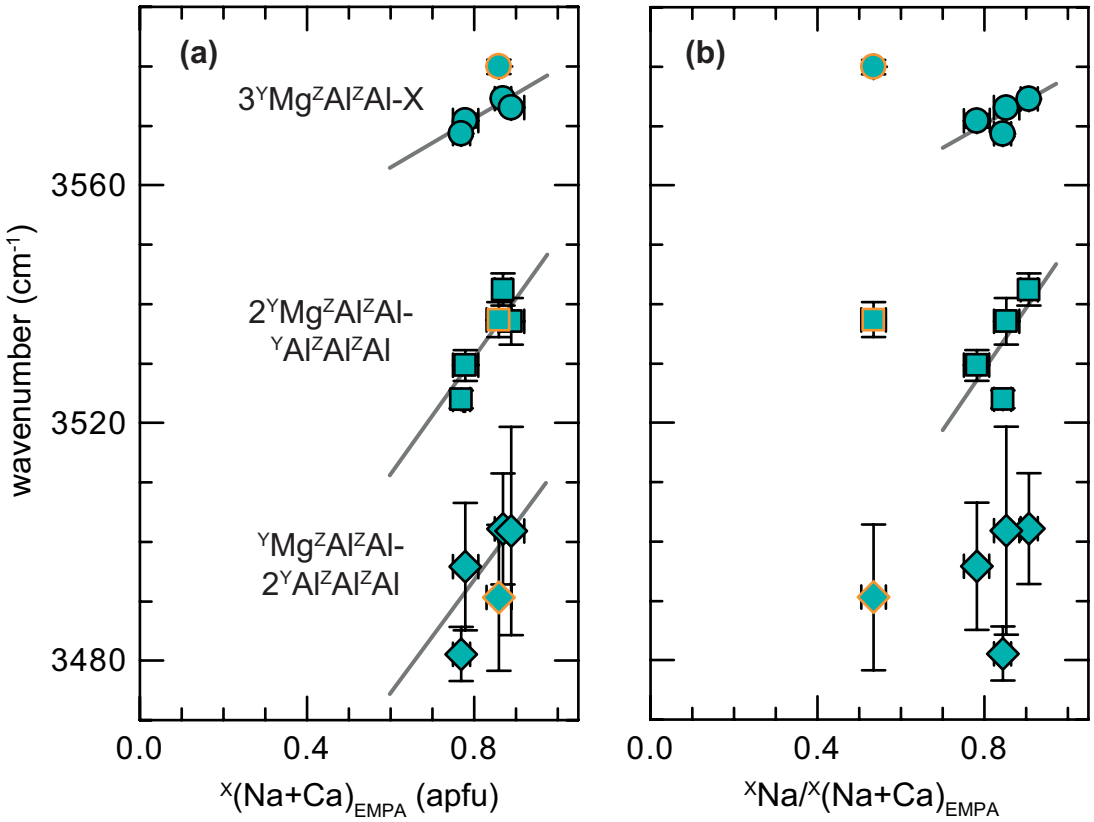
(a)
(b)
3YMgZAlZAl-X
2YMgZAlZAl-
YAlZAlZAl
YMgZAlZAl-
2YAlZAlZAl
wavenumber (cm-1)
3560
3520
3480
0.0
0.4
0.8
X(Na+Ca)EMPA (apfu)
XNa/X(Na+Ca)EMPA

Figure 10

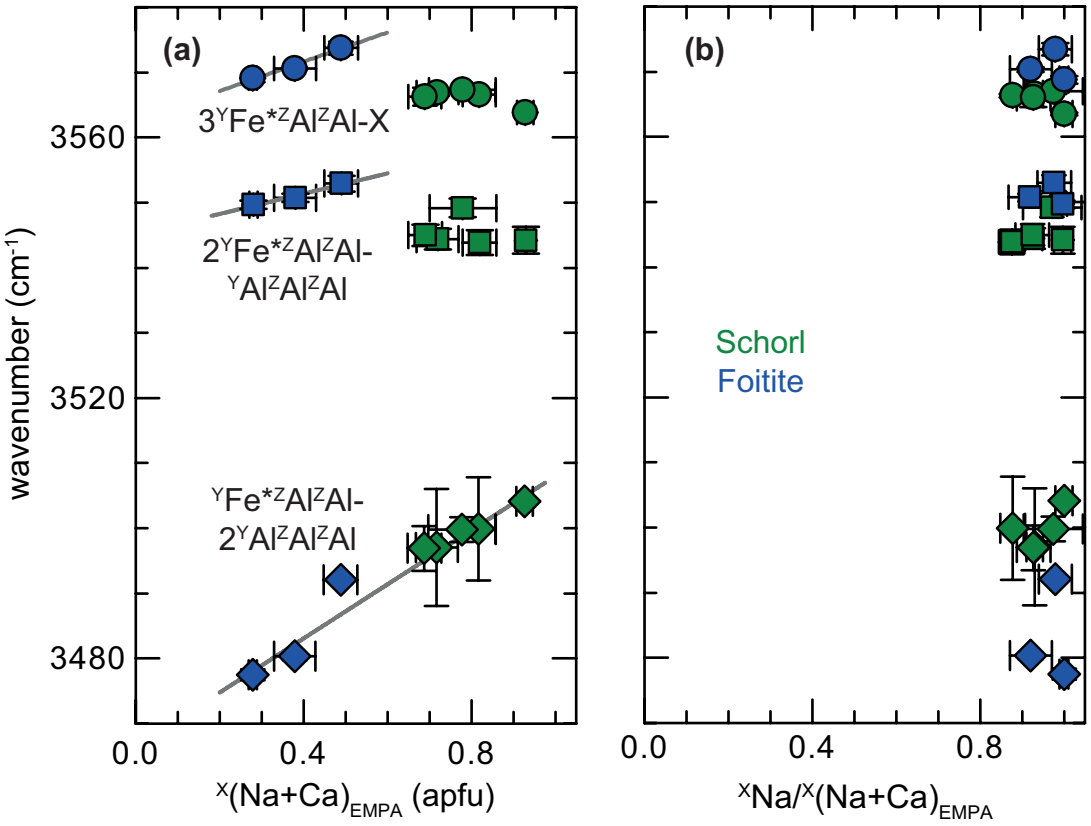
(a)
(b)
3YFe*ZAlZAl-X
2YFe*ZAlZAl-
YAlZAlZAl
YFe*ZAlZAl-
2YAlZAlZAl
Schorl
Foitite
wavenumber (cm-1)
3560
3520
3480
0.0
0.4
0.8
X(Na+Ca)EMPA (apfu)
XNa/X(Na+Ca)EMPA

Figure 11

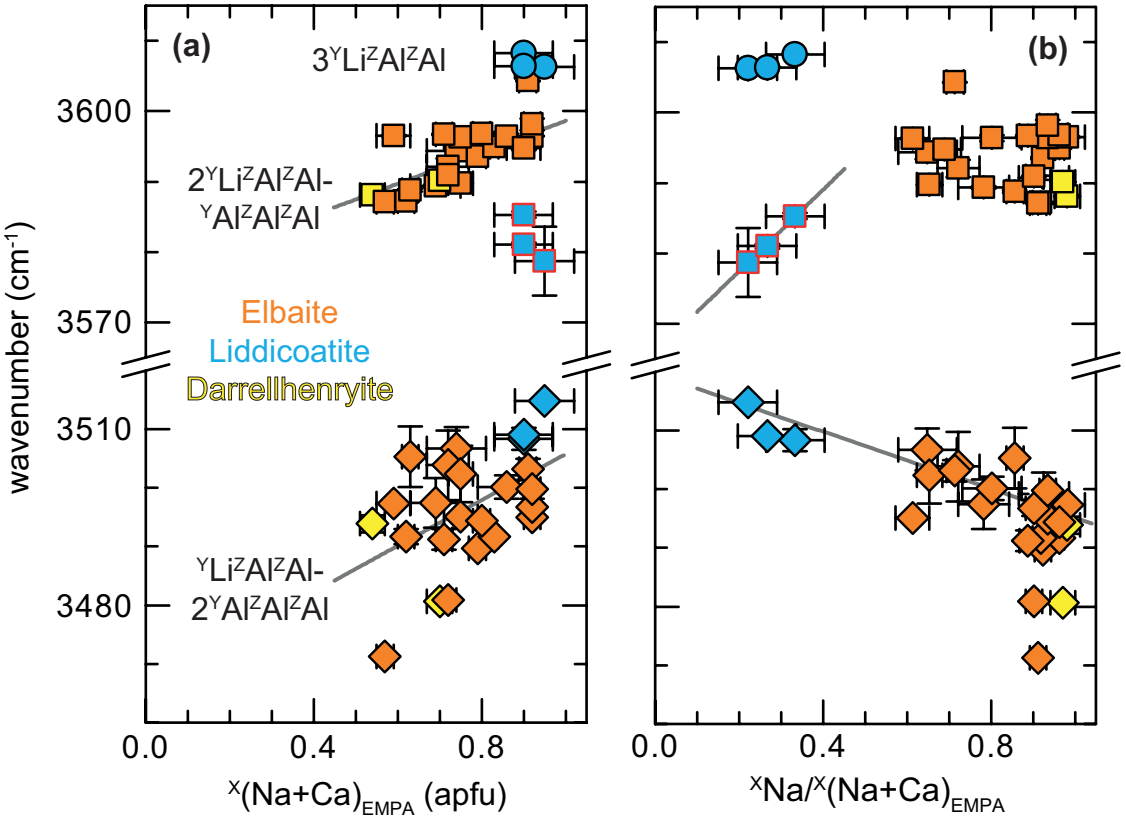
(a)
(b)
3YLiZAlZAl
2YLiZAlZAl-
YAlZAlZAl
YLiZAlZAl-
2YAlZAlZAl
Elbaite
Liddicoatite
Darrellhenryite
wavenumber (cm-1)
3600
3570
3510
3480
0.0
0.4
0.8
X(Na+Ca)EMPA (apfu)
XNa/X(Na+Ca)EMPA